Science Advances
AAAS

Manuscript Template

FRONT MATTER

Title: Land Subsidence on Java Island and Its Contributions to Relative Sea Level Change
Short Title: Land Subsidence and Sea Level Rise on Java Island

Authors

Leonard O. Ohenhen[1]*, Manoochehr Shirzaei[2,3], Praveen Kumar[4,5], Arif Aditiya[6], Ashutosh Tiwari[7], James Davis[8], Folarin Kolawole[8], Estelle Chaussard[9], Nitheshnirmal Sadhasivam[2], Oluwaseyi Dasho[2], Wen Zhong[2], Roselyn H. James[10], Samuel Daramola[11], Robert J. Nicholls[12,13], Philip S.J. Minderhoud[14,15,16]

Affiliations

[1]Department of Earth Systems Science, University of California, Irvine, USA.
[2]Department of Geosciences, Virginia Tech, USA.
[3]Instutute of Water, Environment and Health, United Nations University, Canada.
[4]Department of Earth and Planetary Sciences, Rutgers University, Piscataway, NJ, USA.
[5]Rutgers Climate and Energy Institute, Rutgers University, New Brunswick, NJ, USA.
[6]Geospatial Information Agency, Indonesia.
[7]Texas A&M AgriLife Research Center, Corpus Christi, TX, USA.
[8]Lamont-Doherty Earth Observatory of Columbia University in the City of New York, New York, NY, USA.
[9]FM, USA.
[10]10Alytics, Leicester, UK.
[11]Department of Civil and Environmental Engineering, Virginia Tech, Blacksburg, VA, USA.
[12]Tyndall Centre for Climate Change Research, University of East Anglia, Norwich, UK.
[13]School of Engineering, University of Southampton, Southampton, UK.
[14]Soil Geography and Landscape Group, Wageningen University and Research; Wageningen, The Netherlands.
[15]Department of Civil, Environmental and Architectural Engineering, University of Padova; Padova, Italy.
[16]Department of Subsurface and Groundwater Systems, Deltares Research Institute; Utrecht, The Netherlands.

***Corresponding author:** oohenhen@uci.edu

Abstract

Rising sea levels and land subsidence combine to determine relative sea-level (RSL) rise, which is intensifying coastal hazards. However, many densely populated regions lack the observational infrastructure to identify and quantify land subsidence contribution to RSL, hindering effective planning of responses. Here, we utilized satellite radar observations to generate a high-resolution assessment of land subsidence across Java Island, Indonesia, and evaluate its contribution to 21st-century RSL change. We identify widespread and temporally evolving subsidence with rates ranging from 1-15 cm per year in multiple coastal cities. Using machine learning spatiotemporal clustering and ancillary datasets, we attribute the dominant subsidence mechanisms to resource extraction across various geographic and geological settings. We further construct virtual tide gauges at 5-km intervals along the northern coastline, revealing that contemporary subsidence will dominate RSL budgets over the next 25 years along >75% of the coast. These findings underscore the urgent need to integrate subsidence into sea-level risk and adaptation assessments in vulnerable coastal regions.

Teaser

Land subsidence will drive up to 85% of relative sea-level rise along Java's coast by 2050, outpacing global ocean rise.

MAIN TEXT

Introduction

Globally, low-elevation coastal zones face an escalating array of natural hazards that threaten infrastructure, livelihoods, and ecosystems (*1-3*). These areas are subject to a confluence of acute events such as tropical cyclones, extratropical cyclones and storm surges (*4*), extreme rainfall (*5*), and wave inundation events (*6*); alongside chronic stressors such as shoreline erosion (*7,8*), saltwater intrusion (*9*), and recurrent tidal flooding (*5,6*) that progressively degrade coastal environments and communities through instantaneous, persistent, and incremental impacts (*3,6,10*). Together, these processes generate compound, spatially variable, and temporally evolving risks that demand both short-term emergency responses and long-term adaptation strategies that balance immediate protection and risk reduction with long-term sustainable development goals (*11*).

Central to these evolving risks is the interaction between the rising sea surface and vertical land motion (VLM) (*12*). Their combined effect determines relative sea-level (RSL) change (*13*), a key determinant of flood exposure, drainage capacity, and shoreline stability (*3,10,14*). While sea-level rise driven primarily by climatic effects of thermal expansion, ocean mass changes associated with ice mass loss, and glacial isostatic adjustment create spatially variable oceanic changes worldwide (*3,15*), RSL rise reflects localized conditions experienced at the coast. In many locations, land subsidence (i.e., negative VLM), often anthropogenically driven, can exceed oceanic processes by an order of magnitude (*12,16,17*). This distinction is critical, as land subsidence amplifies RSL rates at local scales, accelerating chronic hazards and exacerbating exposure to acute events (*6,12,17,18–20*). While the relative contributions of oceanic and terrestrial processes vary widely across spatial and temporal scales (*15*), accurately quantifying this heterogeneity requires an integrated observational framework that simultaneously accounts for oceanographic dynamics and land-surface deformation (*3,21*).

However, tide gauge networks essential for measuring long-term RSL trends and capturing the combined effects of ocean processes and VLM remain sparsely distributed across global coastlines, especially in low- and middle-income nations where coastal vulnerability is often greatest due to rapid urbanization and limited adaptation capacity (*22,23*). For example, only 18 Permanent Service for Mean Sea Level (PSMSL) stations from the African continent provide observational data for understanding current and projected regional sea-levels in the IPCC 6th Assessment Report (AR6), while the 130,000 km South-eastern Asia coastline hosts just 49 stations (*24*). Similarly, the limited availability of Global Navigation Satellite System (GNSS) stations further constrains our ability to resolve the highly heterogeneous subsidence patterns that dominate RSL variability. These observational infrastructure gaps leave vast stretches of vulnerable coastline without sufficient long-term observational data to assess current and future local RSL dynamics. Furthermore, because VLM rates can vary significantly over short distances, even dense *in situ* observation networks are insufficient on their own to accurately quantify RSL.

Java island, Indonesia – home to ~2% of the global population (150 million inhabitants) – represents a critical hotspot where these challenges converge, creating an archetype of compound coastal vulnerability driven by both climate and anthropogenic factors (*25*) (Fig. 1). The Java Sea exhibits absolute sea-level rise rates of 5 – 6 mm per year since 2000 (Fig. 1), while urban subsidence in cities like Jakarta reaches up to 15 cm per year (Refs. *26,27*). The resulting RSL rise rates far surpass global projections, transforming long-term risks into an immediate threat for millions of people. However, this predominant narrative of "Jakarta is sinking" (*26,28*), has obscured the broader, island-wide impacts. Existing studies have documented land subsidence in major urban centers across the island (*26,27,29–31*), particularly along the northern low-lying

coastline – a densely populated corridor that is the country's economic and population hub extending approximately 1,500 km. With projected sea levels along this coastline potentially reaching 1 m by the end of the century (Fig. 1B–D), the vulnerability of this region could be significantly magnified by subsidence. While previous studies documented land deformation patterns across Java (*27,31*), these studies have relied on single satellite orbit geometries, limiting comprehensive attribution of spatio-temporal deformation trends. This knowledge gap is further enhanced by Indonesia's lack of representation in the PSMSL stations used for IPCC AR6 sea level projections (although local monitoring stations may exist but are not publicly accessible).

In this study, we address these knowledge gaps by developing a comprehensive island-wide assessment of land subsidence patterns across Java Island and evaluating its contribution to RSL rise along the northern coastline. We quantify both the spatial extent and temporal evolution of subsidence hotspots using satellite geodetic measurements, classify the dominant anthropogenic drivers, and construct historical and projected 21st century RSL trends at 5 km resolution along the northern coast. Additionally, we introduce a process-based approach to interpreting drivers of land motion, shifting from static rate maps to a dynamic understanding of hazard evolution. Our findings provide critical insights for risk assessment, adaptation planning, and sustainable long-term urban development across the region, supporting more targeted and effective responses in the face of intensifying coastal risks.

Results

Spatio-temporal Variability of Land Subsidence on Java Island

To estimate the spatial and temporal trends of land subsidence across Java, we employed a multitemporal interferometric synthetic aperture radar (InSAR) approach to ~4,000 SAR images from 10 ascending and 11 descending frames acquired by the Sentinel-1 C-band satellite from 2017 to 2023 (Fig. 2; table S1). We combined these SAR datasets with VLM rates inferred from GNSS observations at 28 sites to generate 75 m spatial resolution 2D displacement fields of horizontal (east-west) (fig. S1) and VLM (Fig. 2A) across the Island (see methods).

The horizontal land motion in a local reference frame exhibits negligible average velocity (< 0.1 cm per year) across the island, reflecting overall stability (fig. S1). However, localized zones of enhanced east-west horizontal motion with peak velocities of up to 1 cm per year, are observed in urban centers such as Jakarta, Bekasi Regency, Bandung, and Semarang (fig. S1B-D). These zones of elevated horizontal displacement correlate with urban centers and areas experiencing high subsidence rates (>5 cm per year) (Fig. 2A) and coincide spatially with previously documented cases of structural damage to buildings, roads, and other infrastructure (*29,32*). Regions of high spatially variable horizontal displacement and subsidence rates are associated with localized crustal strain, which can induce hogging and sagging effects in structures–bending deformations that lead to cracking, tilting, and structural failure (*33*).

The VLM data across Java indicates widespread subsidence at an average rate of -0.5 cm per year and a standard deviation of 1 cm per year, indicating notable spatial variability across the island (Fig. 2A). We identify hotspots of high subsidence rates (>1 cm per year) in coastal and inland urban centers, including Jakarta, Bekasi, Bandung, Tegal, Semarang, Cilacap, Surabaya, Sidoarjo, and Jember. Other rapidly subsiding non-urban regions include Pekalongan, northern Subang, Brebes, Madiun, Demak, areas adjacent to the Lusi mud volcano, and large agricultural fields along the Bengawan Solo River in Pasi village, Lamongan Regency. Detailed analysis of VLM distributions for 12 major districts reveals that more than 20% of the urban area in the majority of these cities (9 out of 12) is subsiding faster than 1 cm per year, and in Bandung, Pekalongan, and Demak, over 30% of the city area is experiencing subsidence rates greater than 5 cm per year (fig. S2). In the majority of these 12 cities, mostly located along the northern

coastline, we observe median subsidence rates of more than 0.5 cm per year and peak subsidence rates exceeding 10 cm per year (table S2). Analysis of the spatially varying VLM along the northern coastline shows that more than 25% of the 1,500 km stretch of the coastline (defined as a 10 km buffer extending inland from the shoreline) is experiencing subsidence at rates greater than 1 cm per year, with the most severe sinking concentrated in low-lying elevation and highly populated regions (Fig. 2B). The hotspots of subsidence exposure (high subsidence rate, high population, and low elevation) along the coastline (within ~1 km inland) include Jakarta (maximum subsidence: 3.6 cm per year; population: 100,000 people; average elevation: 0.1 m), Cirebon (maximum subsidence: 3.8 cm per year; population: 12,000 people; average elevation: 0 m), Pekalongan (maximum subsidence: 10 cm per year; population: 5,000 people; average elevation: -0.1 m), and Semarang (maximum subsidence: 8 cm per year; population: 10,000 people; average elevation: -0.1 m).

Furthermore, we characterize the temporal evolution of VLM at each InSAR pixel as accelerating, decelerating, or monotonic (linear). For this, we applied a time-dependent quadratic regression model to the Sentinel-1 VLM time series to quantify recent nonlinear trends (see methods; figs. S3A and S4). We then tested for the existence of a significant nonlinear pattern in the VLM data using a t-test ($p < 0.05$), ensuring that acceleration or deceleration trends were statistically significant (see methods). To examine long-term changes in subsidence rates, we compared historical VLM rates from ALOS-1 L-band satellite data (2007–2010) (Ref. *27*) with the Sentinel-1 estimates, classifying locations where land subsidence has intensified, remained stable, or slowed relative to past trends (see methods; fig. S3B). Our analysis reveals that 17% of currently subsiding areas exhibit statistically significant acceleration in VLM over the short timescales (2017–2023), while 45% show a deceleration in the subsidence rate (Fig. 2C). Along the coastline, the accelerating subsidence trend is concentrated in some high-population regions such as Cirebon (mean acceleration: 0.2 – 1.0 mm per year^2), Tegal (0.2- 0.4 mm per year^2), and central Semarang (0.5 – 2.0 mm per year^2), whereas we observe linear or decelerating trends in Jakarta, Demak, Surabaya, and Sidoarjo (Fig. 2B). Analysis of the long-term trends reveals that ~13% of previously identified subsiding zones have transitioned from moderate subsiding conditions (<0.5 cm per year) in the late 2000s to rapid subsidence over the past decade (Fig. 2D). These intensifying trends are observed mostly in urban areas such as Bekasi, Tegal, Pekalongan, Semarang, Bandung, and Madiun, as well as other rural areas including Pamanukan, and agricultural areas in Demak and Pasi, with mean subsidence rate increasing by 1 – 7 cm per year (fig. S3B). In contrast, slowed subsidence or reversed trends are observed in 22% of the land area, notably in areas of central Jakarta, Cirebon, Cilacap, Surabaya, and several rural districts, which may reflect the effects of localized subsidence control efforts such as reduced groundwater extraction. The remaining 65% of the land area exhibited no notable change in subsidence rates over the past decade, indicating persistent deformation at rates comparable to those observed in the late 2000s (Fig. 2D).

Comparison of these long-term trends with annual flood extent (2012–2023) derived from VIIRS (Visible Infrared Imaging Radiometer Suite) observations indicates that regions experiencing a transition from stable to subsiding conditions or where subsidence has intensified, such as Madiun, Pekalongan, Demak, and Pasi, also exhibit concurrent increases in the rate of flood frequency and extent (fig. S5).

Dynamics and Attribution of Subsidence Hotspots on Java Island

To investigate the spatial clustering of subsidence patterns (i.e., contiguous areas with consistent deformation characteristics) and their underlying drivers across Java Island, we implemented a hybrid unsupervised machine learning framework that integrates temporal variability in VLM, spatial proximity, and dynamic deformation behavior, followed by post hoc interpretation using geospatial and geologic datasets and previous studies (see methods; fig. S6).

This approach leverages the complementary strengths of temporal pattern analysis and spatial contextualization to delineate cohesive subsidence zones with physically distinct deformation patterns. To that end, we first applied k-means temporal clustering on the horizontal and vertical displacement time series after dimensionality reduction using principal component analysis (PCA) to isolate dominant temporal trends between 2017 and 2023. Next, we refined the spatial coherence of the clusters using Density-Based Spatial Clustering of Applications with Noise (DBSCAN) to aggregate adjacent pixels from shared temporal clusters into contiguous spatial units based on a 1-km neighborhood radius and a subsidence threshold (>0.5 cm per year). Finally, we employed multivariate dynamic time warping (DTW) to compare the mean detrended cluster time series, identifying regions with analogous temporal structure (e.g., delayed onset, curvature, inflection points, or phase shifts).

The k-means clustering revealed seven dominant temporal patterns, partitioned by Density-Based Spatial Clustering of Applications with Noise (DBSCAN) into 30 spatially coherent deformation clusters (Fig. 3A and fig. S7). These clusters capture the primary deformation hotspots across the Island, each with unique spatiotemporal deformation characteristics (Fig. 3A and figs. S7 and S8).

Cluster 0, comprising areas with background VLM rates (<-0.5 cm per year) and minimal spatial coherence (<5 km), was excluded from further analysis. Broadly, we find that multiple clusters overlap spatially, likely reflecting shared land deformation driving processes across different areas. In the Western Java region, eight spatial clusters (Clusters 5, 6, 7, 8, 9, 12, 13, and 15) co-occur within a 600 km^2 zone, extending from Banten–Jakarta to eastern Bekasi Regency (fig. S7B). Similarly, six clusters (Clusters 1, 2, 3, 4, 17, and 21) concentrate along Central Java's northern coastline in Cirebon, Beres, Tegal, Pekalongan, Semarang, and Demak (fig. S7A). Other multi-cluster regions include the Sidoarjo-Surabaya metropolitan area and Jember Regency (Clusters 23, 24, 29) occupy the narrow southern coastal region (fig. S7D). Apart from Cluster 29, cluster-level east-west motion shows a median rate of 0 cm per year while the median VLM rates vary significantly (median ranging from -1 to -7 cm per year; standard deviation: 0.3 to 8 cm per year) (fig. S8).

To classify shared deformation behavior, we grouped the 29 spatial clusters into six (6) distinct spatiotemporal groups using multivariate dynamic time warping (DTW) (Fig. 3B and fig. S9). Lower DTW distances reflect greater similarity in temporal evolution, while higher distances indicate divergent behaviors. A DTW distance threshold of 200 was selected to balance inter-group dissimilarity and intra-group cohesion. Below we discuss the deformation characteristics of the 6 distinct groups with inferred drivers interpreted from their temporal signatures, spatial distribution, regional geological and anthropogenic contexts, and comparisons with previous site-specific studies (table S3).

Group 1 exhibits sharp, high-amplitude VLM oscillatory patterns (-1.5 to +2 cm), likely reflecting a complex mixture of spatially heterogeneous surface and subsurface processes (fig. S10). These clusters correspond to agricultural, urban, industrial, and peri-urban regions located on Central Java's coastal alluvial deposits (*34*) (Fig. 3 and fig. S11). The irregular peaks and troughs may suggest asynchronous groundwater use and recharge cycles across the group's spatial footprint. While similar geologic deposits occur in other areas of the Island (fig. S11A), the temporal pattern of group 1 likely reflects the heterogeneous anthropogenic stressors and diverse extraction regimes (*27,35,36*). Group 2 is characterized by multi-year VLM oscillations (-2.5 to +1.5 cm), suggesting deformation patterns modulated by both extraction and natural hydrologic variability (fig. S10). Clusters in group 2 are found predominantly in deltas and along river channels, such as Pamanukan and the Brantas Delta in Sidoarjo, these clusters likely reflect regional climate patterns combined with human extraction responses to those conditions (*27*) (Fig. 3 and fig. S12). Group 3 features moderate-amplitude oscillations (-1 to +1.3 cm) with mild

seasonal variability and no extreme amplitudes, characteristic of residential zones experiencing consistent but modest land motion driven by domestic groundwater usage (fig. S13). Although the spatial and temporal characteristics of Group 3 strongly suggest groundwater withdrawal as the dominant mechanism, contributions from shallow or deep sediment compaction cannot be ruled out. These clusters are distributed across urban residential zones such as central Jakarta, parts of Bandung, and Jember regency (*26,27,29*). Group 4 displays the least seasonal variation among all the groups (-1 to +1 cm) but exhibits a monotonic downward trend, suggesting continuous accelerating subsidence (fig. S10). These clusters are mostly located in industrial zones or mixed industrial and residential areas like Jakarta, Bekasi, Bandung, and Surabaya (figs. S12B and D). The temporal trend of this group may reflect deformation associated with sustained, intensive deep aquifer resource (likely groundwater or hydrocarbon) extraction (*27, 37*) (Fig. 3 and fig. S13). Group 5 is characterized by large-amplitude seasonal oscillations (-3 to +2 cm), repeating temporal fluctuations representative of seasonal groundwater depletion and recharge linked to irrigation practices (*37*) (fig. S10). Group 5 is primarily observed in the agricultural zones along the Bengawan-Solo River plains in Pasi and agricultural fields in Madiun (Fig. 3 and fig. S12C). Lastly, group 6, corresponding to the Lusi mud volcano in Sidoarjo (Fig. 3B), exhibits complex, episodic, nonlinear vertical (-1.5 to +1.8 cm) and horizontal (-1.5 to +3.2 cm) motion (amplitude ratio = 0.7) possibly indicative of anthropogenic signals superimposed on natural (tectonic) deformation events (*38*) (figs. S10A and B).

Collectively, these spatiotemporal groups reveals that land subsidence across Java Island is driven by several key mechanisms: intensive groundwater withdrawal in urban coastal centers including Jakarta, Bekasi, Semarang, and Surabaya (Groups 3-4), seasonal agricultural extraction cycles (Group 5), natural sediment compaction and loading in deltaic environments such as Pamanukan and the Brantas Delta (Groups 1-2), and mixed anthropogenic-tectonic processes (Group 6) (Fig. 3B).

Relative Sea Level along the Northern Coastline of Java Island

We quantified 21st century historical, present, and future (projected) RSL change along the northern coastline of Java Island by combining InSAR-derived VLM estimates with absolute sea level trends and probabilistic sea level projections to create time-resolved virtual tide gauge records at 5 km intervals along the coastline (see Methods). For historical (2001–2013) and present-day (2014–2024) RSL estimates, we integrated gridded satellite altimetry data with satellite-derived VLM rates to create spatial dense fields of observed RSL trends. For future projections (2024 to 2050), probabilistic projections of RSL were obtained using the Framework for Assessing Changes to Sea-level (FACTS) (*39*), presented as medium and low confidence under multiple emission scenarios (SSPs 1-1.9, 1-2.6, 2-4.5, 3-7.0, 5-8.5). The VLM component incorporated into FACTS is assumed to be temporally stable (linear projection) over the next two decades, while we also explored potential sensitivity of the projection to non-linear VLM.

Our analysis reveals substantial spatial heterogeneity in RSL rates across the coastline (Fig. 4). During the historical period, observed RSL rise rates ranged from 0.4 to 8.9 (average: 1.5) cm per year (Fig. 4A). Current RSL rise rates (measured over the past decade) show a notable increase compared to historical measurements, varying between 0.2 to 9.0 (average: 1.7) cm per year, with the highest rates observed in Jakarta, Cirebon, Tegal, Pekalongan, Semarang, and Demak (Fig. 4B). These elevated rates above historical measurements reflect increases in the land subsidence rates (5–100%) over the past decade, despite a decrease in sea level trends over the same period (1–70%) (fig. S14). By 2050, under SSP2-4.5 (current emissions trajectory), projected RSL rates are expected to reach 0.4 to 9.0 (average: 1.8) cm per year. These rates represent a two- to ten-fold increase compared to those attributable to sea-level rise alone (fig. S14).

Fig. 5 presents the virtual tide gauge records for multiple areas in four representative coastal cities (Jakarta, Cirebon, Semarang, and Surabaya) (see data S1 for all locations). Across these locations, cumulative RSL shows an increase between 0.1 to 0.7 m since 2001 (start of the 21st century). The current short-term trajectories across 70% of the locations align most closely with either SSP1-2.6, representing a low-emissions pathway, or SSP2-4.5, an intermediate-emissions scenario. By 2050, RSL is projected to rise by 0.4 to 1.9 m across all scenarios (17th to 83rd percentile), with the likely range for SSP2-4.5 being 0.5 to 1.7 m, relative to the year 2001. Under low-confidence assumptions, SSP5-8.5 projections by 2050 approach 2.0 m in Jakarta, Cirebon, and Semarang. Incorporating temporally evolving VLM patterns alters projected RSL rates and trajectories under SSP2-4.5, producing differences in the rates exceeding 1 cm per year and RSL change between 0.3–0.7 m by 2050 (figs. S15 and S16).

To assess the relative contributions of various processes to RSL change along the coastline, we quantified the fractional contributions of climate-related (sterodynamic, glaciers, and ice sheet mass) and non-climatic (VLM and land water storage) driven components. Currently, VLM dominates the RSL budget, accounting for 25–91% of total RSL change under the high-emissions scenario (SSP5-8.5) (medium confidence) across 77% of the coastline (Fig. 6A). Over short timescales (projections by 2050), VLM remains the primary driver in over 75% of coastal segments, contributing 27–85% of total RSL variability, particularly in densely populated urban centers (Fig. 6B and C). Sterodynamic effects – primarily thermal expansion and regional ocean circulation shifts – and glacier loss constitute the second-largest driver but contribute less than 25% to the total RSL budget across the coastline. Ice sheet mass loss contributes minimally (<20% combined), while changes in terrestrial water storage (e.g., groundwater, reservoir fluxes) play a negligible role (<1%) in RSL variance across all time horizons and segments.

Discussion

Java Island's coastal plains are experiencing RSL rise at rates that exceed regional and global averages, driven by the compounding interplay of climate-driven oceanic processes and natural or anthropogenically accelerated land subsidence. The Java Sea shows current (2001 to 2024) rates of 5–7 mm per year, which is 25–75% higher than the global mean (Fig. 1). However, our analysis reveals that land subsidence rates of 1–15 cm per year dominate present and presumably future RSL budgets along much of the densely populated northern coastline, outpacing present and predicted climate-driven sea-level rise rates even under the highest-emission scenarios. These findings align with global observations that local land subsidence currently acts as the primary driver of increasing coastal vulnerability in some low-elevation regions, with south, east and southeast Asia being major hotspots (*12,17*). This hazard is amplifying the threat to Java Island's coastal and inland areas far beyond Jakarta's well-documented coastal challenges, compromising critical infrastructure, intensifying present-day chronic flooding, exacerbating 21st century flood exposure, and enhancing socioeconomic and environmental risks across the region.

For Java's coastal and inland urban areas, land subsidence also emerges independently as a severe hazard to infrastructure, driving systemic risks that extend beyond RSL. As the ground progressively sinks, critical infrastructure networks such as water supply lines, transportation routes, energy grids, and building foundations are strained to the point of failure (*33, 40*). While vertical displacement directly undermines structural stability, lateral ground motion (or horizontal motion)–often underappreciated in infrastructure risk assessments–may induce differential shearing, tilting, and stress accumulation in buildings and linear infrastructure (*33*). We observed these dual modes of ground deformation in Jakarta, Bandung, and Semarang (Fig. 2A; fig. S1), where damage manifests as warped roads and rail lines, ruptured pipelines, and multi-level structural failure (*29,32, 41*). Land subsidence also subverts flood-management systems,

compromising the physical integrity of protective infrastructure such as levees, seawalls, and drainage networks, making flood management policies and approaches misaligned with present-day reality (*20,42*). Coastal regions that stood above high tide just a few decades ago are now routinely inundated during normal high tides, even in the absence of rainfall, while inland cities face their own variants of flood risk exacerbation as subsidence alters drainage gradients and amplifies runoff exposure (*43*) (fig. S5). In Semarang, for example, banjir rob (tidal flooding) has evolved from a sporadic nuisance into a chronic crisis, inundating roads and submerging homes (*44*). Similarly, in Bandung, subsidence along the Citarum River has reduced channel gradients, slowing drainage and trapping floodwaters in industrial and residential zones already burdened by aging infrastructure (*29*). These examples highlight a widespread challenge around the world, where land subsidence reinforces multiple dimensions of vulnerability, emphasizing the need for integrated and sustainable subsidence management, forward-looking urban planning, and adaptive flood control strategies in coastal regions that consider all the climate and non-climate drivers of risk (*11,42,45,46*).

In cases where subsidence is anthropogenically driven, local and city-specific groundwater policies, governance capacity, and infrastructure systems can offer effective solutions that reshape subsidence trajectories (*16, 45*). On Java Island, the observed geographic distribution of VLM reveals both encouraging transitions and concerning new patterns. In parts of Jakarta, our analysis shows a current decelerating trend and a shift from rapid subsidence during 2007 – 2010 to near stability or even uplift in 2017 – 2023 in 50% of the land areas (Fig. 2 and fig. S3A). This transition coincides with the phased implementation of groundwater extraction bans in high-risk zones, industrial relocation incentives, and expansion of piped water infrastructure to reduce aquifer dependence (*47*) (fig. S13A). This demonstrates that regulatory and economic measures can halt or even reverse human-induced subsidence trajectories as shown in other Asian locations (*48*). In addition to this policy-driven recovery, we also observe a natural uplift of the land (~2 mm per year) in the Ciliwung River delta region east of Jakarta (Fig. 2A), likely reflecting sediment deposition or possibly elastic unloading processes, highlighting the diverse VLM mechanisms operating across the region. Yet these localized gains contrast with the emergence of new subsidence hotspots elsewhere on the island. As regulations tightened in core urban centers, groundwater extraction and water-intensive industries (e.g., agricultural areas) appear to have migrated to peri-urban and rural regions as observed previously around Bangkok, Thailand (*49*). Our analysis reveals accelerating or emerging subsidence trends in previously stable districts of Madiun, Jember, and Pasi, which previously showed minimal deformation (Fig. 2; figs. S3A and B). This pattern suggests a concerning "balloon effect" and a critical gap in subsidence policy and management, where subsidence is not being eliminated but merely displaced geographically, transforming once-stable areas into zones with high rates of RSL rise, infrastructural stress and increased socioeconomic and environmental degradation.

The compounding effects of land subsidence and sea-level rise create a dual hazard for many coastal communities, which poses challenges for observational monitoring and predictive modeling of coastal risk, particularly as the subsidence component is underappreciated. A major limitation lies in the sparse and uneven global distribution of observational networks (tide gauges and GNSS), restricting both the spatial resolution and coverage of RSL observations (*21,22).* Even where measurement stations exist, they typically offer only point measurements, providing limited spatial coverage of complex coastal systems and failing to capture the heterogeneous nature of both land and oceanographic processes (*20*). This limitation is particularly consequential in urban centers, where human activities drive variable land motion in space and time, producing different relative sea-level conditions along short coastal transects. Our analysis, along with other recent studies (*50, 51*), demonstrates that satellite observations can overcome these limitations, providing a framework for creating virtual tide gauges at high spatial resolution across most

coastal zones, thereby enhancing the detection of RSL hotspots that are likely to remain undetected by conventional monitoring networks.

Beyond recent uncertainty quantification of non-linearity in VLM trends (*51,52*), we show that VLM exhibits complex temporal behaviors (linear, accelerating, and decelerating phases) that are not captured by standard linear projections. This variability has direct implications for sea-level projections, as extrapolations based on historical linear trends can significantly under- or overestimate future RSL change. Our sensitivity analysis reveals that in some locations, linear versus nonlinear projections diverge by over 40 cm by 2050, underscoring the importance of considering temporal dynamics in risk assessment and adaptation planning (figs. S15 and S16). Developing scenario-based, driver-specific subsidence projections–methodologically aligned with existing multi-scenario sea-level frameworks–represents an important direction for future research (*17, 45*), which would equip decision-makers with a more realistic range of land-surface change futures for planning effective adaptive responses.

Worldwide, the widespread confluence of accelerating land subsidence and sea-level rise is reshaping coastal risks, demanding a paradigm shift in risk assessment and adaptation strategies. The systemic archetypes revealed in our analysis demonstrate that growth engines like resource extraction must be constrained to prevent cascading hazards across water, land, and infrastructure systems. Thus, maintaining and enhancing resilience in subsidence-prone coastal regions requires reallocating limited adaptation resources to prioritize subsidence mitigation measures along with broader coastal adaptation strategies (*11,53,54*). Without such integration, coastal communities risk perpetuating cycles of maladaptation, where short-term infrastructural fixes inadvertently accelerate long-term vulnerabilities by creating false impressions of security while baseline hazards continue to intensify.

Materials and Methods

Land Surface Deformation on Java Island

SAR Interferometric Analysis

We utilized synthetic aperture radar (SAR) datasets from the Sentinel-1 C-band satellite to generate surface land deformation dataset for Java Island, Indonesia. The SAR datasets include 4,000 images acquired in ascending and descending orbit geometries spanning 2017 to 2023. The datasets contain 10 and 11 frames for the ascending and descending satellite orbits, respectively (Fig. 1 and table S1). For each SAR frame, we employed a multitemporal SAR interferometric approach to create the surface deformation time series in the satellite's line-of-sight (LOS) using Wavelet-Based InSAR (WabInSAR) algorithm (*55,56*). We applied a multi-looking factor of 32 in range and 6 in azimuth directions, resulting in a pixel resolution of ~75 m. We first performed coregistration of the SAR images using precise ephemeris orbit data and Shuttle Radar Topography Mission digital elevation model (DEM) and apply an enhanced spectral diversity (ESD) algorithm to minimize the interferometric phase error (*57*). Next, we generated over 11,000 interferograms from the coregistered SAR images using the GAMMA software (*58*), employing a pair selection algorithm optimized via dyadic temporal downsampling and Delaunay triangulation (*59*). The interferometric pairs were constrained to a maximum threshold of 150 m for perpendicular and 300 days for temporal baselines, respectively, to minimize decorrelation errors. Next, we retained so-called elite pixels with average coherence greater than 0.7 for distributed scatterers and amplitude dispersion less than 0.35 for permanent scatterers using a statistical framework (*59*). We then unwrapped the interferogram phases of the elite pixels using a 2D minimum cost flow algorithm (*60*) optimized for sparse coherent pixels (*61*). We corrected all unwrapped interferograms for the effect of orbital error (*62*) and reduced the effects of spatially uncorrelated topography error and the topography-correlated component of atmospheric delay

(*55,63*). To estimate the LOS time series and rates of each pixel, we use a reweighted least-squares optimization (*55,56*), using stable GPS-affiliated or stable zero-velocity pixels as local reference point. The final LOS for each SAR frame is mosaiced to generate two large-scale maps of LOS displacements for the ascending and descending datasets, following the approach detailed in (*64*).

2D Land Motion Decomposition

Given the satellite's near-polar orbit geometry, which provides minimal sensitivity to north-south motion, we decompose the LOS time series into two components of land motion – horizontal (east-west) and vertical (VLM) – by jointly inverting the ascending and descending datasets (*40*). Consequently, we first resampled the LOS displacement data from the descending track onto the location of pixels within the ascending dataset by identifying co-located pixels within a 10 m spatial radius. Let $\{y_A,\ y_D\}$ and $\{\sigma_A^2,\ \sigma_D^2\}$ be the LOS displacement and associated variances for a given pixel, respectively, where the subscripts A and D denote ascending and descending track geometries. The model for the horizontal (d_e) and vertical (d_v) components of displacement is expressed in Equation (1) and solved using a weighted least- squares adjustment, given in Equation (2).

$$\begin{bmatrix} y_A \\ y_D \end{bmatrix} = \begin{bmatrix} C_A^e & C_A^v \\ C_D^e & C_D^v \end{bmatrix} \begin{bmatrix} d_e \\ d_v \end{bmatrix} \quad (1)$$

$$X = [G^T P G]^{-1}\, G^T P L \quad (2)$$

C is the unit vector for projecting the 2D displacements $\{d_e, d_v\}$ onto the LOS (*65*), X is a matrix of unknowns $\{d_e, d_v\}$, L are the observations $\{y_A,\ y_D\}$, G is a design matrix, and P is a weight matrix, the elements of which are inversely proportional to the observant variances (σ^2).

After obtaining the 2D displacement for each pixel, we performed an affine transformation to translate the vertical velocities to the IGS14 global reference frame (*64,66*). We used the vertical velocities of 10 global navigation satellite systems (GNSS) stations (35% of the available GNSS data) provided by the Nevada Geodetic Laboratory (*67*) and previous studies (*30*). The final VLM and east-west rates are shown in Fig. 2 and fig. S1, respectively. Note that the east-west velocity is provided in the local reference frame.

Error Analysis, Temporal Variability, and Validation of VLM Measurements

We evaluated the precision of the displacement velocities using the associated parameter uncertainties (i.e., standard deviation), quantified the temporal variability in VLM trends, and validated the VLM rate estimates by comparison against GNSS vertical observation. We employ the concept of error propagation (*68*) to obtain the variance-covariance matrix (Q_{XX}) using Equation (3):

$$Q_{XX} = [G^T P G]^{-1} \quad (3)$$

The standard deviations (formal uncertainties) for VLM and east-west velocities are shown in fig. S17. In addition to the formal uncertainties, we quantify temporal variability in the d_v by estimating the posterior uncertainty associated with d_v at each observation epoch. For each time step t_i, the standard deviation characterizes the uncertainty in the estimated d_v, capturing deviations from a linear trend. The temporal variability for each pixel is defined using Equation (4):

$$\sigma_{temporal} = \frac{1}{n}\sum_{i=1}^{n} \sigma_{d_v}(t_i) \quad (4)$$

where n is the total number of time steps. This metric offers a quantification of time-dependent deformation behavior, distinguishing temporally variable motion from steady or linear displacement patterns (fig. S18).

To validate the VLM rates, we compared the VLM rates in IGS14 reference frame with VLM observations from 26 available GNSS stations (including GNSS observations utilized for aligning the reference frame). The comparison shows a correlation of 0.83 – 0.96 and a mean and standard deviation of 0.1 and 0.4 cm per year, respectively, for the difference between the two datasets (fig. S19).

Analysis of Multi-Epoch VLM Trends

To evaluate the temporal evolution of VLM, we implemented a dual-epoch trend analysis that separately characterizes (1) recent short-term accelerations or decelerations in VLM, and (2) long-term changes in VLM trends over decadal timescales.

For the short-term (2017–2023) analysis, we modeled the time-dependent displacement at each InSAR pixel using the quadratic polynomial in Equation (5) to identify accelerating, decelerating, or monotonic (linear) deformation patterns:

$$d_u(t) = \frac{1}{2}at^2 + vt + \varepsilon(t) \quad (5)$$

where $d_u(t)$ is the cumulative vertical displacement, a is the acceleration in cm per year², v is the velocity in cm per year, and $\varepsilon(t)$ represents the observation error. To ensure the robustness of our analysis, we tested for the existence of a statistically significant ($p < 0.05$) nonlinear pattern in each time series using a t-test. If a statistically significant relationship exists, we classify the pixels by the sign of a into accelerating (positive) or decelerating (negative) subsidence trends, and assign "linear" if the test fails to reject the null hypothesis.

For the long-term (multi-epoch) analysis, we compared contemporary VLM rates derived from Sentinel-1 observations (2017–2023) with historical rates derived from ALOS-1 L-band data spanning 2007–2010. The ALOS-1 dataset was obtained from Chaussard et al. (*27*), which applied InSAR observations to map VLM trends across Java and parts of Sumatra Islands, Indonesia. After resampling the ALOS-1 measurements to the Sentinel-1 pixels, we computed the velocity difference for each pixel using Equation (6):

$$\Delta v = v_S - v_A \quad (6)$$

Where, v_S is the VLM rate derived from Sentinel-1 observations, and v_A is the corresponding rate from the ALOS-1 dataset. Based on the magnitude and sign of Δv, we adopted the scheme in Equation (7) to classify the subsidence trends as intensifying/emergent (IE), stable (ST), or slowing (SL).

$$\Delta v = \begin{cases} IE & if\ \Delta v < -0.5\ cm\ per\ year \\ ST & if\ |\Delta v| \leq 0.5\ cm\ per\ year \\ SL & if\ \Delta v > 0.5\ cm\ per\ year \end{cases} \quad (7)$$

We selected these thresholds to account for systematic variations in processing methodologies between the two datasets, differences in the orbit geometries, and to accommodate the measurement uncertainties inherent in the ALOS-1 observations. This comparison enabled identification of areas where land subsidence has worsened, stabilized, or improved over the past decade (figs. S3 and S4) – reflecting both policy-driven interventions (e.g., groundwater regulations) and emergent stressors from expanding urban and resource demand (fig. S13).

Classification and Attribution of Deformation Hotspots on Java Island

To identify and characterize dominant patterns of land deformation across Java Island, we developed a hybrid unsupervised machine learning framework that integrates temporal dynamics of deformation, spatial contiguity of subsiding regions, and multivariate time series comparison of the deformation trends. The objective of this classification was to delineate spatio-temporal coherent subsidence hotspots and to attribute these deformation behaviors to plausible underlying anthropogenic and geophysical/natural drivers. Information mining methods using machine learning have proven valuable for extracting contextual insights from InSAR-derived deformation data, including detection of deformation signals (*69*), spatial, context-driven interpolation (*70*), and decomposition of complex signals into physically meaningful modes (*71–73*). We implemented a four-step methodology (fig. S6): (1) principal component analysis (PCA) for reducing dimensionality in the displacement time series; (2) k-means temporal clustering refined with Density-Based Spatial Clustering of Applications with Noise (DBSCAN) to identify spatially contiguous deformation zones; (3) multivariate dynamic time warping (DTW) to quantify temporal similarities among clusters; and (4) the resulting deformation trends are interpreted using ancillary datasets including geospatial and geologic information, and domain-specific contextual interpretation from previous studies to identify underlying physical drivers and their attribution.

First, we applied PCA to the VLM and east-west displacement time series derived from the Sentinel-1 datasets to extract their dominant temporal features. PCA transformed the original time series into an orthogonal feature space dominated by the principal modes of variability (*74*). For each pixel, the first two principal components explaining ≥90% of the cumulative variance were retained, preserving both long-term and short-term variability while providing a compact representation of deformation signals for subsequent clustering. Next, we applied *k*-means clustering to the PCA-reduced data to group pixels with similar temporal deformation profiles. The *k*-means algorithm partitions the dataset into disjoint *K* clusters by minimizing intra-cluster variance:

$$J = \sum_{k=1}^{K} \sum_{x_i \in C_k} \|x_i - \mu_k\|^2 \quad (8)$$

where x_i is the 2D PCA-transformed feature vector for pixel i, and μ_k is the centroid of cluster C_k. We determined 7 optimal *K* based on the elbow method, yielding clusters with consistent intra-group temporal behaviors. While this step generated clusters reflecting temporal similarity, spatial contiguity was not enforced, leading to fragmented groupings. To ensure spatial continuity and remove noisy outliers, we refined temporal clusters using DBSCAN (*75*). The DBSCAN algorithm aggregates spatially connected pixels with similar deformation patterns into contiguous regions by connecting clusters to density-reachable neighbors. We used a spatial search radius of 5 km and a minimum subsidence threshold of 0.5 cm per year, yielding 30 spatially coherent clusters, each representing distinct temporal and spatial footprint (Fig. 3 and figs. S7 and S8).

To compare temporal deformation trends across the 30 clusters, each cluster was represented by its mean time series. The VLM component was detrended to accentuate short-term variability and structural features such as curvature, inflection points, and seasonal variations associated with anthropogenic processes (e.g., seasonal groundwater extraction), while the east-west displacement retained its original trend to preserve geophysically meaningful horizontal signals (e.g., tectonic signals). Each cluster was then represented as a multivariate time series vector in Equation (9):

$$X^j = \left[v_t^j, e_t^j\right]_{t=1}^{T} \quad (9)$$

Where v_t^j and e_t^j represents average VLM and horizontal displacement at time t for cluster j, respectively.

We then quantified the inter-cluster similarity in deformation behavior between pairs of clusters using DTW (*76*). Unlike univariate DTW, multivariate DTW considers both deformation channels simultaneously, aligning sequences to minimize cumulative Euclidean distance across both vertical and horizontal dimensions. Given two clusters 1 and 2, represented by time series $X^{1,2} = \left\{\left(v_t^{(1,2)}, e_t^{(1,2)}\right)\right\}_{t=1}^{T}$, the DTW distance between them is defined by Equation (10):

$$DTW(1,2) = \min_{\pi} \sum_{(i,j)\epsilon\pi} \left\| X_i^{(1)} - X_j^{(2)} \right\|_2 \quad (10)$$

Where π represents the optimal warping path aligns points in time between the two sequences (1) and (2), $\|\cdot\|_2$ is the Euclidean norm over the 2D deformation vector, and i and j are the time indices from the two sequences being compared. The resulting pairwise DTW distance matrix between all 29 clusters (excluding Cluster 0) was subjected to agglomerative hierarchical clustering, generating a dendrogram spatiotemporal similarity (fig. S9). In the resulting dendrogram, lower DTW distances indicate higher similarity between deformation trajectories, while higher distances reflect greater dissimilarity. This suggests that clusters that merge at low DTW distances exhibit closely matched deformation dynamics, while those connected at higher thresholds show divergent patterns. A DTW distance threshold of 200 was selected empirically to define six meta-clusters or groups refined by contextual knowledge and ancillary datasets, balancing intra-group cohesion with inter-group separation. The resulting groups reflect common deformation trajectories ranging from steady, gradual trends to multi-phased behaviors even among geographically distant clusters.

We interpreted the physical attribution and underlying drivers of the resulting spatiotemporal groups through *post-hoc* integration of multiple geospatial and geologic datasets and previous studies (*26, 27, 29, 35–38*). Specifically, we obtained geologic data of Indonesia to delineate lithologic information across Java Island (*77*) (fig. S11A). High-resolution Google Earth imagery and land cover dataset (*78*) were used to classify land use patterns across the island and differentiate residential, industrial, and agricultural zones (figs. S11B and S12). Lastly, previous studies were used to independently validate and corroborate the inferred deformation mechanisms. The framework presented here is designed for applicability in data-limited environments where direct measurements of hydrological, geological, or anthropogenic forcing are sparse. Deformation mechanisms are therefore inferred from the integration of spatial patterns, temporal signatures, geological context, and comparison with previous site-specific studies. While this approach provides valuable insights into the most plausible dominant physical processes, some deformation classes may represent mixtures of processes including groundwater withdrawal, shallow or deep sediment compaction, and tectonic contributions that cannot be fully disentangled with current datasets. This represents a common challenge in regional-scale subsidence studies and does not diminish the value of the spatiotemporal classification approach for identifying deformation hotspots and their likely dominant mechanisms.

Estimation of Relative Sea Level Trends across Java's Northern Coastline

We estimated historical (2001–2013), present-day (2014–2024), and future (till 2050) relative sea-level (RSL) rise along the northern coastline of Java Island by integrating satellite-derived VLM rates with absolute sea-level anomalies from satellite altimetry and probabilistic sea-level rise projections. To resolve spatial variability of RSL, we constructed high-spatial resolution (5 km), time-resolved virtual tide gauge records along the coastline.

To estimate the observed RSL change (*historical and present-day* epochs), we combined absolute sea-level anomalies (SLA) from satellite altimetry data with InSAR-derived VLM estimates. The altimetry data was obtained from the Copernicus Marine Environment Monitoring Service (*79*), which provides gridded monthly SLA at 0.25° spatial resolution. The SLA dataset includes all standard corrections, including adjustments for instrumental drift, tidal and atmospheric effects, and geophysical processes (*79,80*). Since the SLA resolution is coarser than our 5-km coastal segment grid spacing, we selected the closest SLA grid point to each coastal segment using a minimum distance spatial proximity threshold. SLA values represent instantaneous absolute sea surface height at each time step (i) and were converted to RSL using the VLM estimates, applied cumulatively as a deterministic, constant-rate process across the SLA time series (s_i).

Let v represent the annual VLM rate assigned to each 5-km coastal segment, and N the number of time steps per year (i.e. N = 12 for monthly SLA dataset). The RSL at each timestep (r_i) is given by Equation (11):

$$r_i = \mathcal{L}_v(s_i) = s_i + \left(\frac{v}{N}\right) \cdot i \tag{11}$$

where $\mathcal{L}_v$ denotes a linear operator applying a cumulative displacement from VLM, distributed uniformly across sub-annual intervals assuming land motion progresses linearly and independently of the SLA signals.

To account for differences in VLM across observational epochs, let v_i represent the VLM rate assigned to time step i, applied as a piecewise-constant function such that $v_i = v_A$ for $i \in [1, T_1]$ (corresponding to 2001 – 2013), and $v_i = v_S$ for $i \in (T_1, T]$ (corresponding to 2014 – 2024). The trend of the reconstructed RSL series for each epoch satisfies Equation (12):

$$\frac{dr}{dt} = \frac{ds}{dt} + v \tag{12}$$

Where $\frac{ds}{dt}$ is the trend of absolute SLA, $\frac{dr}{dt}$ and is the trend of the RSL (fig. S20).

Validation of Virtual Tide Gauge Records

To validate the reconstructed RSL time series, we compared the virtual tide gauge estimates against observations from the Permanent Service for Mean Sea Level (PSMSL) station at Cilacap. Although this station is located on the southern coast of Java and outside the primary analysis domain, the Cilacap tide gauge provides the longest continuous sea-level record in the region and serves as a critical benchmark. We find strong agreement in both temporal structure and magnitude, with a high correlation in trend (ρ = 0.9) and a rate difference of 0.1 mm per year between the virtual tide gauge and the PSMSL record (fig. S21).

For projections of RSL through mid-21st century, we applied the Framework for Assessing Changes to Sea-level (FACTS) (*39*), consistent with the IPCC Sixth Assessment Report (AR6) sea-level rise projections. This framework combines probabilistic projections of oceanographic processes such as thermal expansion (sterodynamics), glacier and ice sheet mass loss, and changes in land water storage with localized VLM to produce site-specific RSL change

under multiple Shared Socioeconomic Pathways (SSPs). We incorporated both the VLM rates and their temporal variability (estimated from Equation (4)), to ensure that local VLM trends and confidence bounds reflect nonlinear land motion in the RSL projections. Following the procedures outlined in Kopp et al. (*39*), we generated full probability distributions of projected RSL for five SSPs (SSP1-1.9, SSP1-2.6, SSP2-4.5, SSP3-7.0, and SSP5-8.5), providing estimates of both medium confidence and low confidence (high-impact outcomes) scenarios. Seven projection workflows, corresponding to different assumptions about ice-sheet dynamics and greenhouse gas forcing, were used to account for deep uncertainty in future sea-level contributions (*39*). To combine these outputs into confidence-bound projections, we constructed probability boxes (p-boxes) in accordance with the AR6 guidance on uncertainty quantification. For medium-confidence RSL projections, we used workflow 1e (based on the emulandice emulator for Antarctic ice-sheet response) and workflow 1f for RSL rates; for low-confidence projections, we used workflows 2e and 2f, respectively. Each coastal segment's projected RSL reflects the cumulative contributions from both oceanographic processes and contemporary (Sentinel-1 derived) land subsidence. We emphasize that in these projections, VLM is assumed to be temporally stable (linear rates), consistent with the current AR6 framework. To investigate the sensitivity of RSL projections to nonlinear land motion, we performed an auxiliary analysis to incorporate VLM accelerations (observed in some parts of the coastline) into the no-VLM p-box output through an additive adjustment sampled from empirical probability distributions (figs. S15 and S16). This highlights the influence of accelerating (or decelerating) land deformation on near-term coastal hazard projections and highlights the limitations of assuming linear subsidence rates in the context of evolving anthropogenic pressures.

While the virtual tide gauge construction provides a valid first-order assessment of RSL change, it relies on several simplified assumptions that introduce limitations. First, the assumption of VLM as a constant, deterministic rate neglects temporal variability, including short-term nonlinear trends driven by anthropogenic processes. For instance, observed accelerations in VLM of 0.1–0.2 cm per year^2 in Pekalongan and Semarang indicate that linear rate assumptions may underestimate past and RSL rise in some subsiding regions (see Fig. 2; figs. S3 and S4). Second, the use of satellite altimetry data–originally optimized for open-ocean conditions–to characterize coastal sea-level anomalies introduces additional uncertainty. Nearshore, sea level is influenced by localized processes such as shelf circulation, riverine input, and tidal amplification, which may decouple coastal sea-level behavior from offshore altimetric signals. Third, in projecting future RSL, the extrapolation of contemporary VLM rates assumes stationarity in subsidence processes, which in practice is unlikely to hold over multi-decadal timescales due to shifting land use, hydrological conditions, or mitigation policies (see discussion section for scenario-based land subsidence alternative). Nevertheless, in regions where long-term tide gauge observations are sparse or absent, the virtual tide gauge framework offers a practical and scalable alternative for generating spatially explicit RSL estimates, especially over the next few decades.

References

1. R. J. Nicholls, A. Cazenave, Sea-level rise and its impact on coastal zones. *Science* **328**, 1517–1520 (2010).
2. J. Hinkel, D. Lincke, A. T. Vafeidis, M. Perrette, R. J. Nicholls, R. S. Tol, A. Levermann, Coastal flood damage and adaptation costs under 21st century sea-level rise. *Proc. Natl. Acad. Sci. U.S.A.* **111**, 3292–3297 (2014). https://doi.org/10.1073/pnas.1222469111
3. M. Oppenheimer, B. C. Glavovic, J. Hinkel, R. van de Wal, A. K. Magnan, A. Abd-Elgawad, R. Cai, M. Cifuentes-Jara, R. M. DeConto, T. Ghosh, J. Hay, F. Isla, B. Marzeion, B. Meyssignac, Z. Sebesvari, Sea Level Rise and Implications for Low-Lying

Islands, Coasts and Communities, in IPCC Special Report on the Ocean and Cryosphere in a Changing Climate (Cambridge University Press, 2019).
4. J. C. M. Dullaart, S. Muis, N. Bloemendaal, M. V. Chertova, A. Couasnon, J. C. J. H. Aerts, Accounting for tropical cyclones more than doubles the global population exposed to low-probability coastal flooding. *Commun. Earth Environ.* **2**, 204 (2021).
5. R. Rahimi, H. Tavakol-Davani, C. Graves, A. Gomez, M. F. Valipour, Compound inundation impacts of coastal climate change: sea-level rise, groundwater rise and coastal precipitation. *Water* **12**, 2776 (2020).
6. P. L. Barnard, K. M. Befus, J. J. Danielson, A. C. Engelstad, L. H. Erikson, A. C. Foxgrover, M. K. Hayden, D. J. Hoover, T. W. B. Leijnse, C. Massey, R. McCall, N. C. Nadal-Caraballo, K. Nederhoff, A. C. O'Neill, K. A. Parker, M. Shirzaei, L. O. Ohenhen, P. W. Swarzenski, J. A. Thomas, M. van Ormondt, S. Vitousek, K. Vos, N. J. Wood, J. M. Jones, J. L. Jones, Projections of multiple climate-related coastal hazards for the US Southeast Atlantic. *Nat. Clim. Chang.* **15**, 101–109 (2025).
7. J. Hinkel R. J. Nicholls, R. S. J. Tol, Z. B. Wang, J. M. Hamilton, G. Boot, A. T. Vafeidis, L. McFadden, A. Ganopolski, R. J. T. Klein, A global analysis of erosion of sandy beaches and sea-level rise: an application of DIVA. *Glob. Planet. Change* **111**, 150–158 (2013).
8. M. I. Vousdoukas, R. Ranasinghe, L. Mentaschi, T. A. Plomaritis, P. Athanasiou, A. Luijendijk, L. Feyen, Sandy coastlines under threat of erosion. *Nat. Clim. Chang.* **10**, 260–263 (2020).
9. K. M. Befus, P. L. Barnard, D. J. Hoover et al., Increasing threat of coastal groundwater hazards from sea-level rise in California. *Nat. Clim. Chang.* **10**, 946–952 (2020). https://doi.org/10.1038/s41558-020-0874-1
10. H. R. Moftakhari, A. AghaKouchak, B. F. Sanders, D. L. Feldman, W. Sweet, R. A. Matthew, A. Luke, Increased nuisance flooding along the coasts of the United States due to sea level rise: Past and future. *Geophys. Res. Lett.* **42**, 9846–9852 (2015).
11. R. J. Nicholls, Adapting to sea-level rise. *Resilience* **13**, 13–29 (2018).
12. R. J. Nicholls, D. Lincke, J. Hinkel, S. Brown, A. T. Vafeidis, B. Meyssignac, S. E. Hanson, J. L. Merkens, J. Fang, A global analysis of subsidence, relative sea-level change and coastal flood exposure. *Nat. Clim. Chang.* **11**, 338–342 (2021).
13. J. M. Gregory, S. M. Griffies, C. W. Hughes, J. A. Lowe, J. A. Church, I. Fukimori, N. Gomez, R. E. Kopp, F. Landerer, G. L. Cozannet, R. M. Ponte, Concepts and terminology for sea level: mean, variability and change, both local and global. *Surv. Geophys.* **40**, 1251–1289 (2019).
14. D. M. FitzGerald, M. S. Fenster, B. A. Argow, I. V. Buynevich, Coastal impacts due to sea-level rise. *Annu. Rev. Earth Planet. Sci.* **36**, 601–647 (2008).
15. T. Frederikse, F. Landerer, L. Caron, S. Adhikari, D. Parkes, V. W. Humphrey, S. Dangendorf, P. Hogarth, L. Zanna, L. Cheng, Y. H. Wu, The causes of sea-level rise since 1900. *Nature* **584**, 393–397 (2020).
16. G. Erkens, T. Bucx, R. Dam, G. De Lange, J. Lambert, Sinking coastal cities. *Proc. Int. Assoc. Hydrol. Sci.* **372**, 189–198 (2015).
17. M. Shirzaei, J. Freymueller, T. E. Törnqvist, D. L. Galloway, T. Dura, P. S. Minderhoud, Measuring, modelling and projecting coastal land subsidence. *Nat. Rev. Earth Environ.* **2**, 40–58 (2021).

18. J. P. M. Syvitski, A. J. Kettner, I. Overeem, E. W. H. Hutton, M. T. Hannon, G. R. Brakenridge, J. Day, C. Vörösmarty, Y. Saito, L. Giosan, R. J. Nicholls, Sinking deltas due to human activities. *Nat. Geosci.* **2**, 681–686 (2009).
19. M. Shirzaei, R. Bürgmann, Global climate change and local land subsidence exacerbate inundation risk to the San Francisco Bay Area. *Sci. Adv.* **4**, eaap9234 (2018).
20. L. O. Ohenhen, M. Shirzaei, C. Ojha, S. F. Sherpa, R. J. Nicholls, Disappearing cities on US coasts. *Nature* **627**, 108–115 (2024).
21. G. Wöppelmann, M. Marcos, Vertical land motion as a key to understanding sea level change and variability. *Rev. Geophys.* **54**, 64–92 (2016).
22. M. Marcos, G. Wöppelmann, A. Matthews, R. M. Ponte, F. Birol, F. Ardhuin, G. Coco, A. Santamaría-Gómez, V. Ballu, L. Testut, D. Chambers, Coastal sea level and related fields from existing observing systems. *Surv. Geophys.* **40**, 1293–1317 (2019).
23. O. A. Dada, R. Almar, P. Morand et al., Future socioeconomic development along the West African coast forms a larger hazard than sea level rise. *Commun. Earth Environ.* **4**, 150 (2023). https://doi.org/10.1038/s43247-023-00807-4
24. B. Fox-Kemper et al., Ocean, Cryosphere and Sea Level Change, in Climate Change 2021: The Physical Science Basis. Contribution of Working Group I to the Sixth Assessment Report of the Intergovernmental Panel on Climate Change (Cambridge University Press, 2021). https://doi.org/10.1017/9781009157896.011
25. F. Yulianto, M. Wibowo, A. Yananto et al., Coastal vulnerability assessment using the machine learning tree-based algorithms modeling in the north coast of Java, Indonesia. *Earth Sci. Inform.* **16**, 3981–4008 (2023). https://doi.org/10.1007/s12145-023-01135-z
26. H. Z. Abidin, H. Andreas, I. Gumilar, Y. Fukuda, Y. E. Pohan, T. Deguchi, Land subsidence of Jakarta (Indonesia) and its relation with urban development. *Nat. Hazards* **59**, 1753–1771 (2011).
27. E. Chaussard, F. Amelung, H. Abidin, S. H. Hong, Sinking cities in Indonesia: ALOS PALSAR detects rapid subsidence due to groundwater and gas extraction. *Remote Sens. Environ.* **128**, 150–161 (2013).
28. S. T. Lee, G. Sihombing, The world's fastest-sinking megacity has one last chance to save itself. *Bloomberg* (2023).
29. H. Z. Abidin, I. Gumilar, H. Andreas, D. Murdohardono, Y. Fukuda, On causes and impacts of land subsidence in Bandung Basin, Indonesia. *Environ. Earth Sci.* **68**, 1545–1553 (2013).
30. S. Susilo, R. Salman, W. Hermawan et al., GNSS land subsidence observations along the northern coastline of Java, Indonesia. *Sci. Data* **10**, 421 (2023). https://doi.org/10.1038/s41597-023-02274-0
31. T. P. Sidiq, I. Gumilar, H. Z. Abidin, I. Meilano, A. Purwarianti, R. Lestari, Spatial Distribution and Monitoring of Land Subsidence Using Sentinel-1 SAR Data in Java, Indonesia. *Appl. Sci.* **15**, 3732 (2025).
32. H. Z. Abidin, H. Andreas, I. Gumilar, I. R. Wibowo, On correlation between urban development, land subsidence and flooding phenomena in Jakarta. *Proc. Int. Assoc. Hydrol. Sci.* **370**, 15–20 (2015).

33. F. Cigna, D. Tapete, Present-day land subsidence rates, surface faulting hazard and risk in Mexico City with 2014–2020 Sentinel-1 IW InSAR. *Remote Sens. Environ.* **253**, 112161 (2021).
34. D. Sarah, L. M. Hutasoit, R. M. Delinom, I. A. Sadisun, T. Wirabuana, A physical study of the effect of groundwater salinity on the compressibility of the semarang-demak aquitard, Java Island. *Geosciences* **8**, (2018).
35. A. Aditiya, T. Ito, Present-day land subsidence over Semarang revealed by time series InSAR new small baseline subset technique. *Int. J. Appl. Earth Obs. Geoinf.* **125**, 103579 (2023).
36. R. Azeriansyah, K. E. Ching, B. D. Yuwono, Impact of Land Subsidence-Induced Three-Dimensional Surface Deformation on Infrastructure in the Semarang-Demak Alluvial Plain, Indonesia. *J. Earth Mar. Technol.* **5**, 111–122 (2025).
37. M. Rygus, M. Bianchi, A. Novellino, E. Hussain, A. Taufiq, S. R. Rusli, C. Meisina, Permanent aquifer storage loss from long-term groundwater withdrawal: A case study of subsidence in Bandung (Indonesia). *J. Hydrol. Reg. Stud.* **57**, 102129 (2025).
38. M. Shirzaei, M. L. Rudolph, M. Manga, Deep and shallow sources for the Lusi mud eruption revealed by surface deformation. *Geophys. Res. Lett.* **42**, 5274–5281 (2015).
39. R. E. Kopp, G. G. Garner, T. H. J. Hermans, S. Jha, P. Kumar, A. Reedy, A. B. A. Slangen, M. Turilli, T. L. Edwards, J. M. Gregory, G. Koubbe, A. Levermann, A. Merzky, S. Nowicki, M. D. Palmer, C. Smith, The framework for assessing changes to sea-level (FActS) v1.0: A platform for characterizing parametric and structural uncertainty in future global, relative, and extreme sea-level change. *Geosci. Model Dev.* **16**, 7461–7489 (2023).
40. L. O. Ohenhen, M. Shirzaei, Land subsidence hazard and building collapse risk in the coastal city of Lagos, West Africa. *Earth's Future* **10**, e2022EF003219 (2022).
41. L. Ley, Building on borrowed time: rising seas and failing infrastructure in Semarang (U of Minnesota Press, 2021).
42. M. Esteban, H. Takagi, L. Jamero, C. Chadwick, J. E. Avelino, T. Mikami, T. Shibayama, Adaptation to sea level rise: Learning from present examples of land subsidence. *Ocean Coast. Manage.* **189**, 104852 (2020).
43. H. Jiang, J. Zhang, Y. Liu, J. Li, Z. N. Fang, Does flooding get worse with subsiding land? Investigating the impacts of land subsidence on flood inundation from Hurricane Harvey. *Sci. Total Environ.* **865**, 161072 (2023).
44. H. Z. Abidin, H. Andreas, I. Gumilar, T. P. Sidiq, Y. Fukuda, Land subsidence in coastal city of Semarang (Indonesia): characteristics, impacts and causes. *Geomat. Nat. Hazards Risk* **4**, 226–240 (2013).
45. P. S. J. Minderhoud, H. Middelkoop, G. Erkens, E. Stouthamer, Groundwater extraction may drown mega-delta: Projections of extraction-induced subsidence and elevation of the Mekong delta for the 21st century. *Environ. Res. Commun.* **2**, 111004 (2020).
46. M. Zhang, R. J. Nicholls, J. Wen, A. AghaKouchak, T. J. Bouma, S. E. Darby, S. Du, Z. Dai, Growing compound-flood risk, driven by both climate change and land subsidence, challenges flood risk reduction in major delta cities. *One Earth* **8**, 101489 (2025).
47. J. Widodo, E. Trihatmoko, N. Setyaningrum, Y. Izumi, R. Handika, M. Ardha, R. Arief, S. Sobue, N. Nurlinda, P. A. Pranantya, J. R. Wiranu, M. R. Khomarudin, Technical and

Policy Analysis: Time Series of Land Subsidence for the Evaluation of the Jakarta Groundwater-Free Zone. *Urban Sci.* **9**, 67 (2025).
48. A. Cao, M. Esteban, V. P. B. Valenzuela, M. Onuki, H. Takagi, N. D. Thao, N. Tsuchiya, Future of Asian deltaic megacities under sea level rise and land subsidence: Current adaptation pathways for Tokyo, Jakarta, Manila, and Ho Chi Minh City. *Curr. Opin. Environ. Sustain.* **50**, 87–97 (2021).
49. N. Phien-wej, P. H. Giao, P. Nutalaya, Land subsidence in bangkok, Thailand. *Eng. Geol.* **82**, 187–201 (2006).
50. T. Naish, R. Levy, I. Hamling, S. Hreinsdóttir, P. Kumar, G. G. Garner, R. Newnham et al., The significance of interseismic vertical land movement at convergent plate boundaries in probabilistic sea-level projections for AR6 scenarios: The New Zealand case. *Earth's Future* **12**, e2023EF004165 (2024). https://doi.org/10.1029/2023EF004165
51. M. Govorcin, D. P. S. Bekaert, B. D. Hamlington, S. S. Sangha, W. Sweet, Variable vertical land motion and its impacts on sea level rise projections. *Sci. Adv.* **11**, eads8163 (2025).
52. J. Oelsmann, M. Marcos, M. Passaro, et al., Regional variations in relative sea-level changes influenced by nonlinear vertical land motion. *Nat. Geosci.* **17**, 137–144 (2024). https://doi.org/10.1038/s41561-023-01357-2
53. J. Fang, R. J. Nicholls, S. Brown, D. Lincke, J. Hinkel, A. T. Vafeidis, S. Du, Q. Zhao, M. Liu, P. Shi, Benefits of subsidence control for coastal flooding in China. *Nat. Commun.* **13**, 6946 (2022).
54. L. O. Ohenhen, G. Zhai, J. Lucy et al., Land subsidence risk to infrastructure in US metropolises. *Nat. Cities* **2**, 543–554 (2025). https://doi.org/10.1038/s44284-025-00240-y
55. M. Shirzaei, A wavelet-based multitemporal DInSAR algorithm for monitoring ground surface motion. *IEEE Geosci. Remote Sens. Lett.* **10**, 456–460 (2013).
56. M. Shirzaei, R. Bürgmann, E. J. Fielding, Application of wavelet-based InSAR time-series analysis for measuring surface deformation in Los Angeles. *J. Geophys. Res. Solid Earth* **120**, 211–227 (2015).
57. M. Shirzaei, R. Bürgmann, E. J. Fielding, Applicability of Sentinel-1 Terrain Observation by Progressive Scans multitemporal interferometry for monitoring slow ground motions in the San Francisco Bay Area. *Geophys. Res. Lett.* **44**, 2733–2742 (2017).
58. C. Werner, U. Wegmüller, T. Strozzi, A. Wiesmann, Gamma SAR and interferometric processing software, *in ERS - Envisat Symposium* (2000).
59. J.-C. Lee, M. Shirzaei, Novel algorithms for pair and pixel selection and atmospheric error correction in multitemporal InSAR. *Remote Sens. Environ.* **286**, 113447 (2023).
60. M. Costantini, A novel phase unwrapping method based on network programming. *IEEE Trans. Geosci. Remote Sens.* **36**, 813–821 (1998).
61. M. Costantini, P. A. Rosen, Phase unwrapping techniques, *in Proceedings of the IEEE International Geoscience and Remote Sensing Symposium (IGARSS)* 267–269 (1999).
62. M. Shirzaei, T. R. Walter, Estimating the effect of satellite orbital error using wavelet-based robust regression applied to InSAR deformation data. *IEEE Trans. Geosci. Remote Sens.* **49**, 4600–4605 (2011).
63. M. Shirzaei, R. Bürgmann, Topography correlated atmospheric delay correction in radar interferometry using wavelet transforms. *Geophys. Res. Lett.* **39**, L01405 (2012).

64. E. Blackwell, M. Shirzaei, C. Ojha, S. Werth, Tracking California's sinking coast from space: Implications for relative sea-level rise. *Sci. Adv.* **6**, eaba4551 (2020).
65. R. F. Hanssen, Radar Interferometry: Data Interpretation and Error Analysis (Kluwer Academic Publishers, 2001).
66. L. O. Ohenhen, M. Shirzaei, C. Ojha M. L. Kirwan, Hidden vulnerability of US Atlantic coast to sea-level rise due to vertical land motion. *Nat. Commun.* **14**, 2038 (2023).
67. G. Blewitt, W. C. Hammond, C. Kreemer, Harnessing the GPS data explosion for interdisciplinary science. *Eos* **99**, EO104623 (2018).
68. E. M. Mikhail, F. E. Ackermann, Observations and Least Squares (IEP Series in Civil Engineering, 1976).
69. N. Anantrasirichai, J. Biggs, F. Albino, D. Bull, The application of convolutional neural networks to detect slow, sustained deformation in InSAR time series. *Geophys. Res. Lett.* **46**, 11850–11858 (2019).
70. A. Radman, M. Akhoondzadeh, B. Hosseiny, Integrating InSAR and deep-learning for modeling and predicting subsidence over the adjacent area of Lake Urmia, Iran. *GISci. Remote Sens.* **58**, 1413–1433 (2021).
71. D. Festa et al., Unsupervised detection of InSAR time series patterns based on PCA and K-means clustering. *Int. J. Appl. Earth Obs. Geoinf.* **118**, 103276 (2023). https://doi.org/10.1016/j.jag.2023.103276
72. M. Rygus et al., A clustering approach for the analysis of InSAR Time Series: Application to the Bandung Basin (Indonesia). *Remote Sens.* **15**, 3776 (2023). https://doi.org/10.3390/rs15153776
73. A. Tiwari, M. Shirzaei, A novel machine learning and deep learning semi-supervised approach for automatic detection of InSAR-based deformation hotspots. *Int. J. Appl. Earth Obs. Geoinf.* **126**, 103611 (2024).
74. H. Hotelling, Analysis of a complex of statistical variables into principal components. *J. Educ. Psychol.* **24**, 417 (1933).
75. M. Ester, H. P. Kriegel, J. Sander, X. Xu, A density-based algorithm for discovering clusters in large spatial databases with noise, *in kdd* **96**, 226–231 (1996).
76. D. J. Berndt, J. Clifford, Using dynamic time warping to find patterns in time series, *in Proceedings of the 3rd international conference on knowledge discovery and data mining* 359–370 (1994).
77. www.indonesia-geospasial.com
78. D. Zanaga et al., ESA WorldCover 10 m 2021 v200 (2022). https://doi.org/10.5281/zenodo.7254221
79. COPERNICUS—Marine Environment Monitoring Service. Available at: http://marine.copernicus.eu/
80. M. Grégoire et al., Monitoring Black Sea environmental changes from space. *Front. Mar. Sci.* **9**, 998970 (2023). https://doi.org/10.3389/fmars.2022.998970

Additional References

81. L. Ma, S. Li, D. Sun, NOAA JPSS Program Office, NOAA JPSS Visible Infrared Imaging Radiometer Suite (VIIRS) Level-3 Global Flood Map from NDE [Data set] (NOAA National Centers for Environmental Information, 2024).
82. S. Aribowo, L. Husson, D. H. Natawidjaja, C. Authemayou, M. R. Daryono, A. R. Puji, P. G. Valla, A. Pamumpuni, D. D. Wardhana, G. de Gelder, D. Djarwadi, M. Lorcery, Active back-arc thrust in north west Java, Indonesia. *Tectonics* **41**, e2021TC007120 (2022).
83. P. Whincup, R. Oktavianus, C. Egy, Jakarta groundwater: victim of its own success. *Hydrogeol. J.* **32**, 353–358 (2024).

Acknowledgments

We thank Meritxell Colet for helpful discussions and valuable insights that contributed to this research. We thank Miguel Silva for help with Figure 3B.

Funding: LOO was supported by LDEO postdoctoral research fellowship. MS, NS, OD, WZ were supported by funding from the Department of Defense.

Author contributions:
Conceptualization: LOO
Methodology: LOO, MS, PK, AT, JD, FK
Investigation: LOO, MS, PK, AT, JD, FK, EC, NS, OD, WZ, RJ, SD, RJN, PSJM
Visualization: LOO
Supervision: LOO
Writing—original draft: LOO
Writing—review & editing: LOO, MS, PK, AT, JD, FK, EC, NS, OD, WZ, RJ, SD, RJN, PSJM

Competing interests: The authors declare they have no competing interest.

Data and materials availability: The vertical land motion and horizontal land motion data for Java Island is available at https://doi.org/10.5281/zenodo.15786356. The Sentinel-1 data used in this study are publicly available through the Alaska Satellite Facility and can be accessed at https://search.asf.alaska.edu. The medium and low confidence projected Relative Sea level change and rates for five SSPs (SSP1-1.9, SSP1-2.6, SSP2-4.5, SSP3-7.0, and SSP5-8.5) is available at https://doi.org/10.5281/zenodo.15786356. The satellite altimetry data for sea level rise is available from Copernicus Marine Environment Monitoring Service (CMEMS) and is available through https://data.marine.copernicus.eu/product/SEALEVEL_GLO_PHY_L4_MY_008_047/download. Access requires the creation of a free CMEMS user account, which is available to all users at no cost upon registration. The population for Java Island was estimated using the WorldPop dataset available through https://hub.worldpop.org/geodata/summary?id=77690. The coastal elevation referenced to mean sea-level uses the DeltaDTM dataset v1.1 available through https://doi.org/10.4121/21997565. All other data needed to evaluate the conclusions in the paper are present in the paper and/or the Supplementary Materials.

Figures and Tables

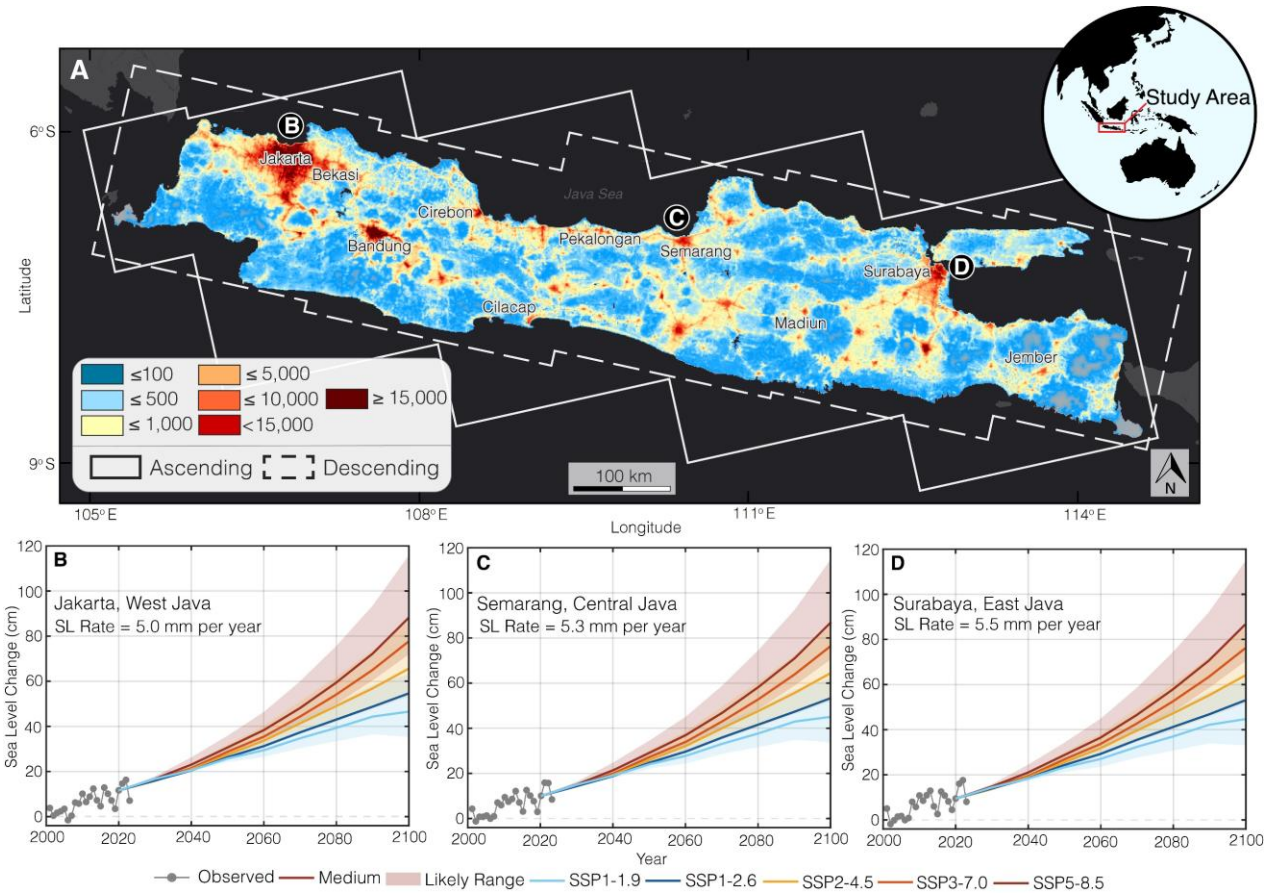

Fig. 1. Study Area and Datasets. (A) Population density (population/km^2) and synthetic aperture radar (SAR) frame boundaries across Java Island. The SAR data includes 10 ascending (solid grey rectangles) and 11 descending (dashed grey rectangles) frames. Observed (2001 – 2024) and projected (2020 – 2050) absolute sea level (ASL) change for **(B)** Jakarta, West Java **(C)** Semarang, Central Java, and **(D)** Surabaya, East Java. The locations of (B), (C), and (D) are shown in (A). The population density data is based on the 2021 WorldPop Global High Resolution Population dataset (WPGP) available through https://www.worldpop.org/. The observed ASL trends (2001 – 2024) are from satellite altimetry dataset obtained from Copernicus Marine Environment Monitoring Service (*79*), while the projected ASL trends (2020 – 2050) are obtained from Fox-Kemper et al. *(24)*. The underlying basemap in (A), is provided by Esri, TomTom, Garmin, FAO, NOAA, USGS.

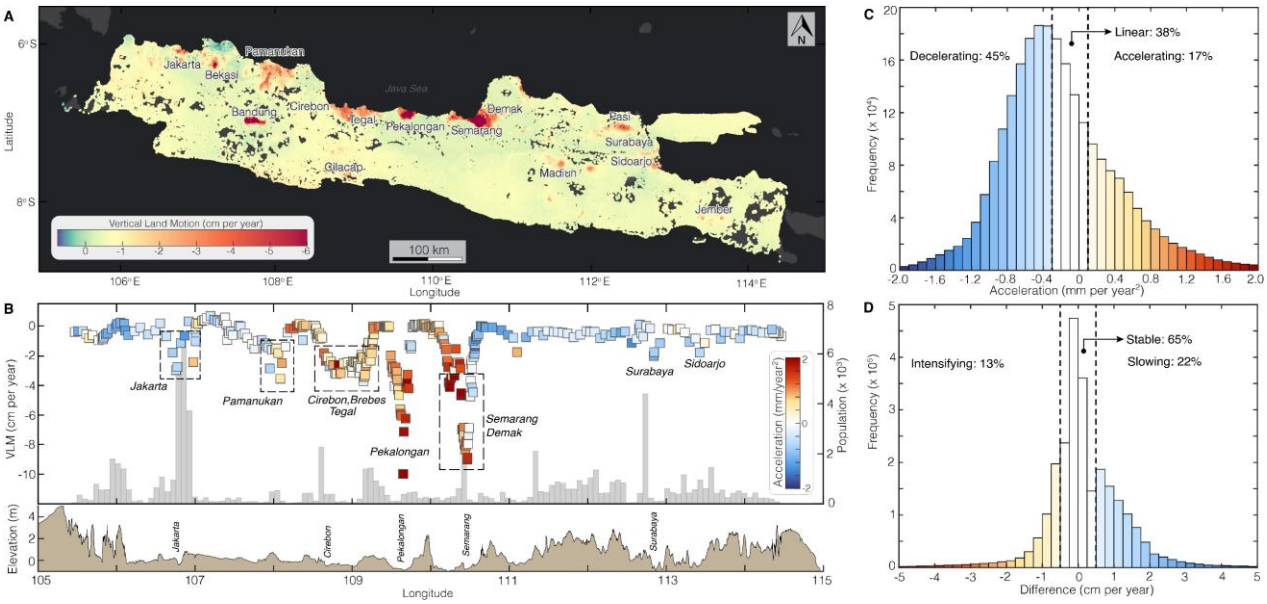

Fig. 2. Spatial Patterns and Temporal Evolution of Land Subsidence across Java Island. (A) Vertical land motion (VLM) rates (2017 – 2023) for Java Island in the IGS14 geodetic reference frame. Negative VLM values indicate subsidence. **(B)** Along-coast transect of VLM sampled at 5-km intervals along the northern coastline, color-coded with acceleration, overlaid on coastal population within 10 km (gray bars). Topography elevation is plotted in the lower panel. Positive acceleration values indicate accelerating subsidence rates, while negative values indicate deceleration. **(C)** Histogram of subsidence acceleration across Java Island, derived from Sentinel-1 observations (2017–2023). The spatial map of the acceleration is shown in fig. S3A. **(D)** Distribution of differences between Sentinel-1 (2017–2023) and ALOS-1 (2007–2011) VLM rates highlighting percentages of intensifying, stable, or slowing subsidence. The spatial map of the difference is shown in fig. S3B. The underlying basemap in (A), is provided by Esri, TomTom, Garmin, FAO, NOAA, USGS.

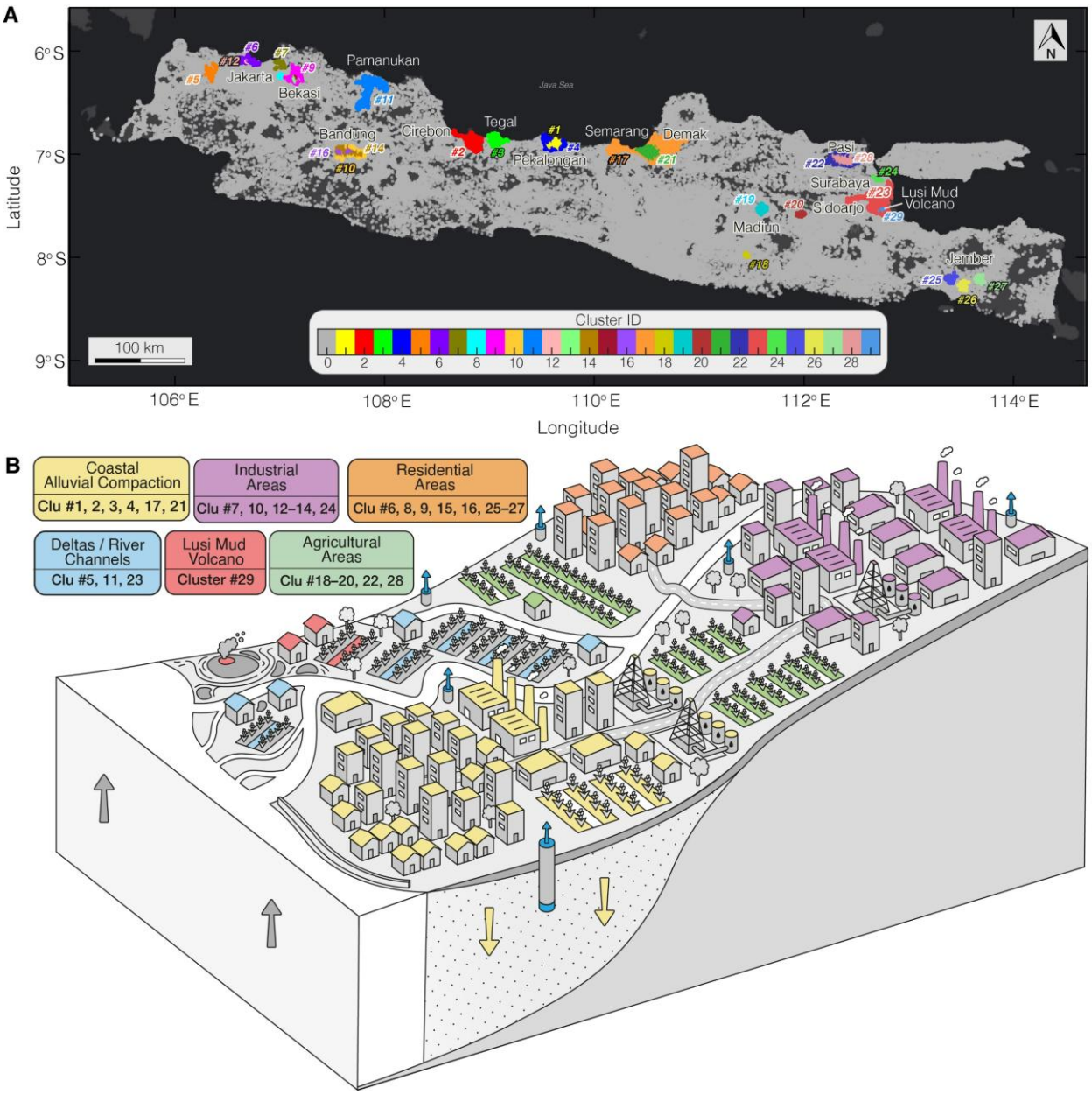

Fig. 3. Spatiotemporal Classification and Attribution of Subsidence Hotspots across Java Island. (A) Spatial distribution of subsidence hotspot derived from k-means clustering of InSAR-derived vertical land motion (VLM) time series and spatial coherence refinement using Density-Based Spatial Clustering of Applications with Noise (DBSCAN). Each color represents a unique cluster (Cluster ID). Detailed figure of each cluster is shown in fig. S9. **(B)** Conceptual model showing the dominant land use or geologic mechanism associated with each group of clusters, determined using multivariate dynamic time warping (DTW) of their temporal signatures. Clusters are grouped into six classes: coastal alluvial compaction (Clusters #1–4, 17, 21), deltas and river channels (Clusters #5, 11, 23), industrial areas (Clusters #7, 10, 12–14, 24), residential areas (Clusters #6, 8, 9, 15, 16, 25–27), agricultural areas (Clusters #18–20, 22, 28), and the Lusi mud volcano (Cluster #29). The underlying basemap in (A), is provided by Esri, TomTom, Garmin, FAO, NOAA, USGS.

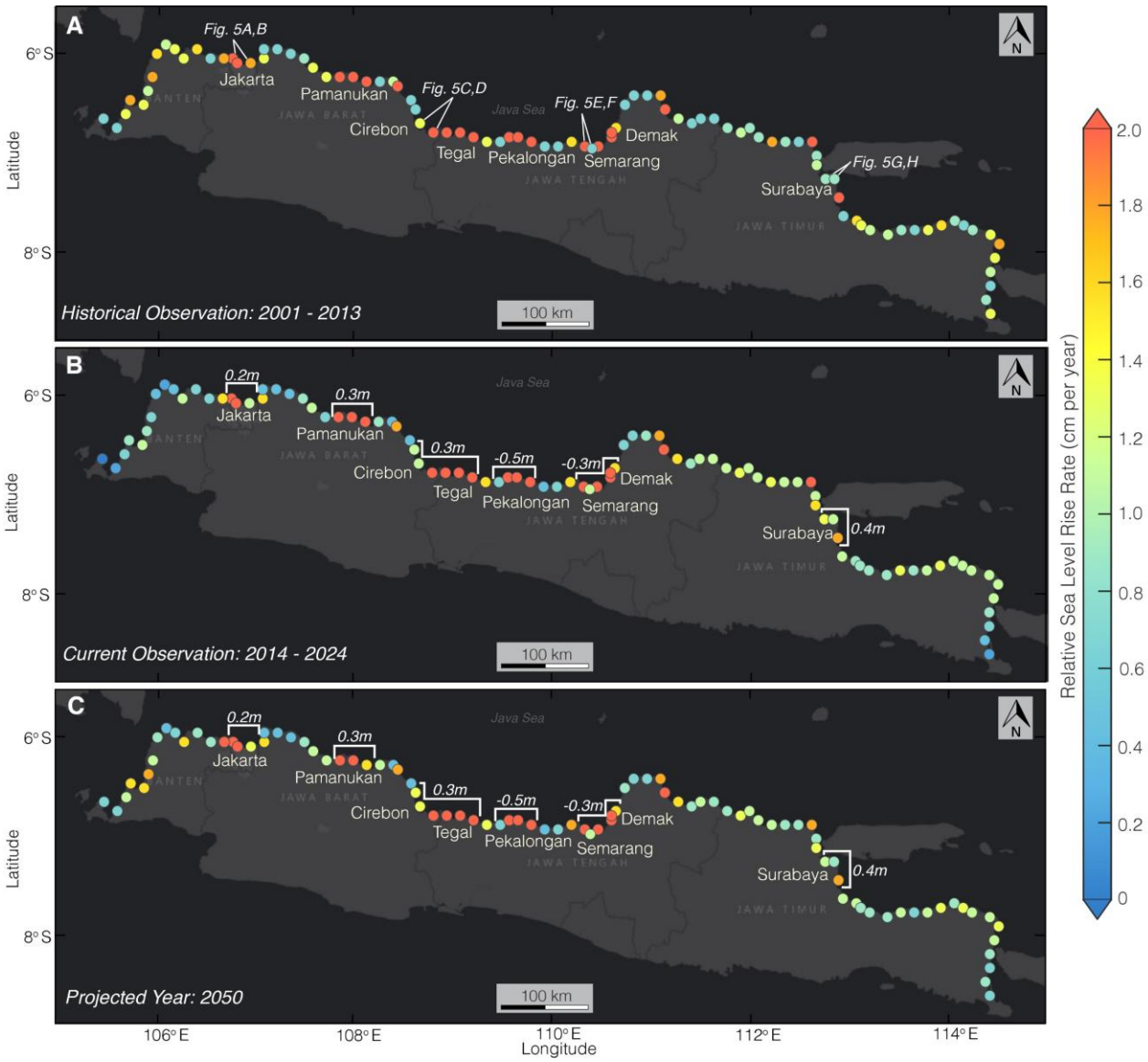

Fig. 4. 21st Century Relative Sea Level (RSL) Rise Rates along the Northern Coastline of Java Island. Observations of RSL rise rates during **(A)** the historical (2001–2013), **(B)** Current (2014 – 2024) periods. **(C)** Projected RSL rise rates under shared socioeconomic pathways 2-4.5 (SSP2-4.5) scenario for the year 2050. Each circle represents a virtual tide gauge constructed at 5 km coastal segments interval. Elevation labels for major coastal cities in panels B and C (Jakarta: 0.2m; Pamanukan: 0.3m; Cirebon and Tegal: 0.3m; Pekalongan: -0.5m, Semarang and Demak: -0.3m; and Surabaya: 0.4m) indicate average elevation relative to mean sea level in meters. The underlying basemap in **(A)** – **(C)** is provided by Esri, TomTom, Garmin, FAO, NOAA, USGS.

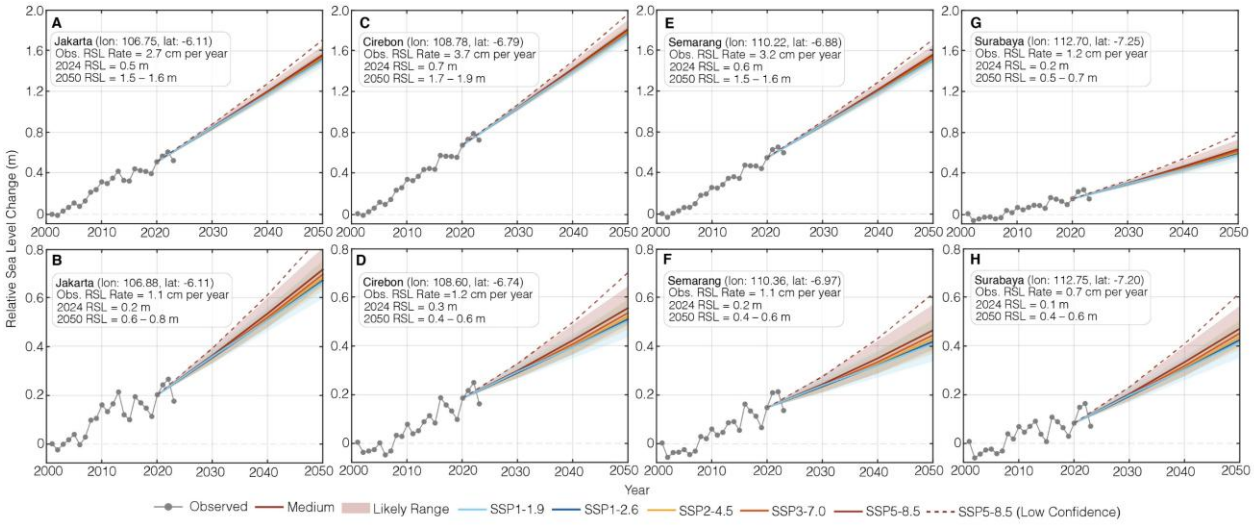

Fig. 5. Relative Sea Level (RSL) Change on Java's Northern Coastline. 21st-century measurements (gray points) and projections till 2050 (blue to red colors and shaded areas) of RSL change for **(A, B)** Jakarta, **(C, D)** Cirebon, **(E, F)** Semarang, and **(G, H)** Surabaya. Projected RSL for five Shared Socioeconomic Pathways (SSPs): SSP1-1.9, SSP1-2.6, SSP2-4.5, SSP3-7.0, and SSP5-8.5 (medium confidence), and SSP5-8.5 (low confidence). Shaded bands represent the likely range (17th and 83rd quantile interval), and bold lines indicate the median (50th quantile) projection. Panels on the top **(A, C, E, G)** represent sites with higher subsidence rates, while those on the bottom **(B, D, F, H)** reflect lower-subsiding or less impacted nearby sites. The time series of the observed monthly trends are shown in fig. S20. The locations of all sites are shown on Fig. 4A.

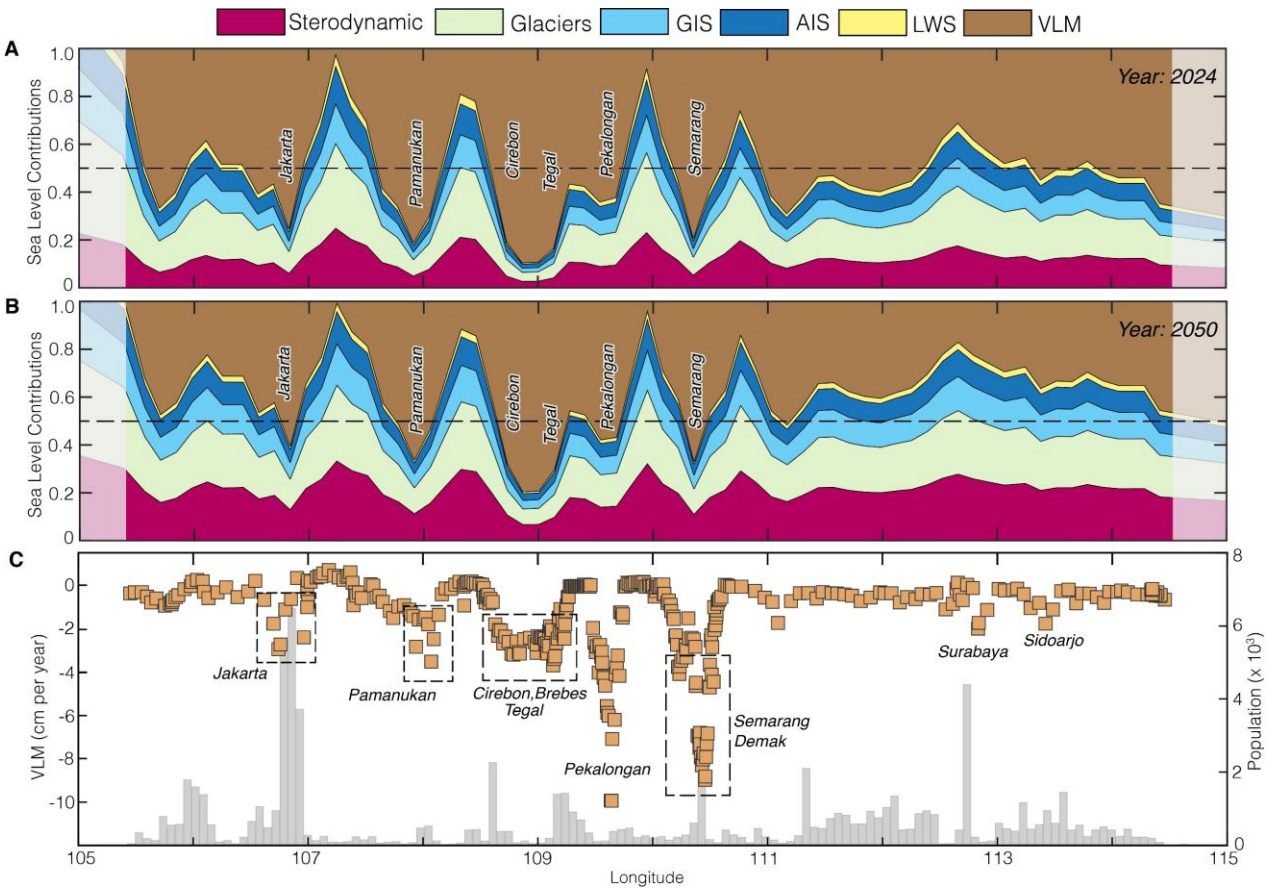

Fig. 6. Component Contributions to Projected Relative Sea Level (RSL) Change along Java's Northern Coastline. Stacked area plots of the fractional contributions of vertical land motion (VLM), land water storage (LWS), Antarctic ice sheet (AIS), Greenland ice sheet (GIS), glaciers, and sterodynamic processes to total projected RSL change at each 5-km coastal segment for the year **(A)** 2024 and **(B)** 2050 under the Shared Socioeconomic Pathways 5-8.5 (SSP5-8.5) scenario (medium confidence). The horizontal dashed line indicates the 0.5 threshold, below which VLM contributes more than half of the total RSL budget. **(C)** Longitudinal distribution of VLM rates, overlaid with coastal population (gray bars).

Supplementary Materials

Please use the *Science Advances* template to format your Supplementary Materials.

ScienceAdvances
AAAS

Supplementary Materials for

Land Subsidence on Java Island and Its Contributions to Relative Sea Level Change

Ohenhen *et al.*

*Corresponding author. Email: oohenhen@uci.edu

This PDF file includes:

Figs. S1 to S21
Tables S1 to S3
Data S1

Other Supplementary Materials for this manuscript include the following:

Data S1

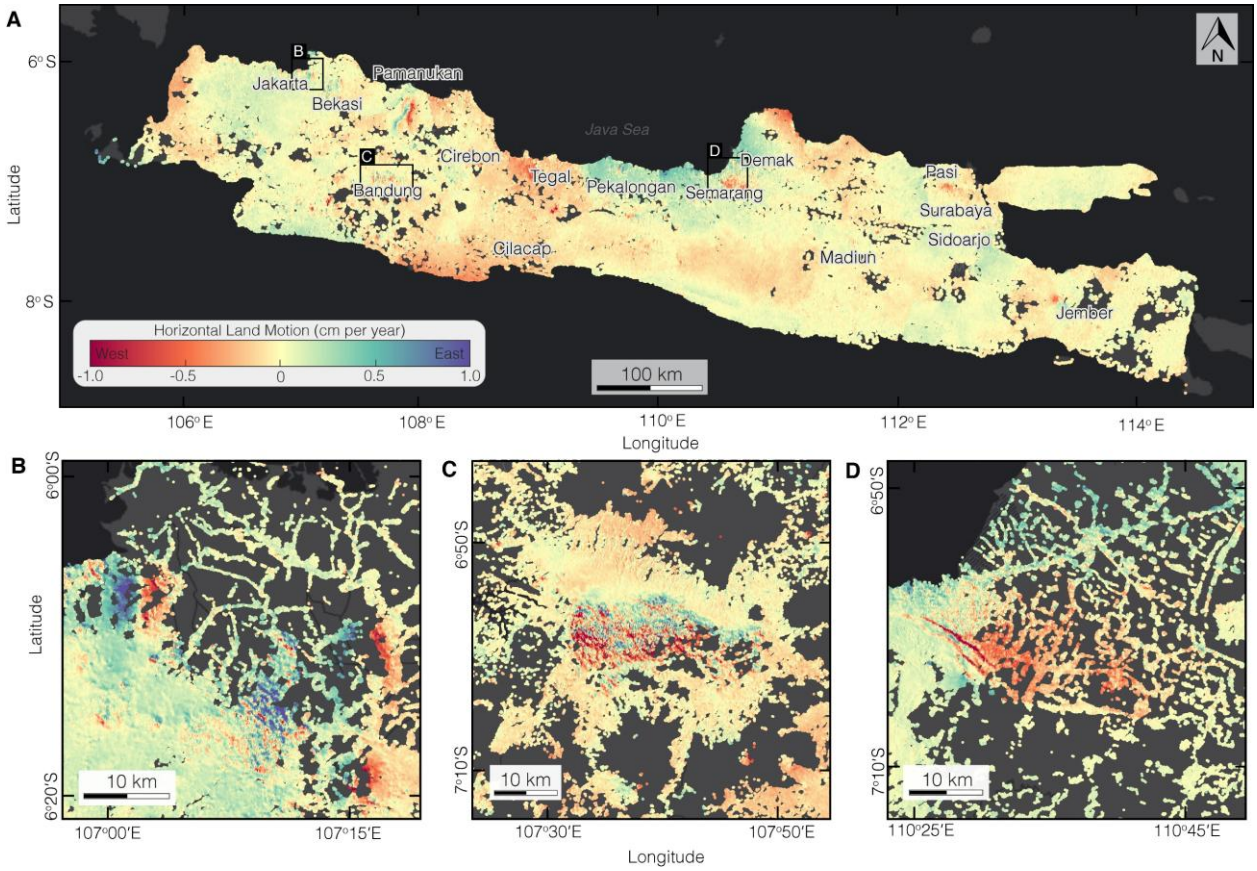

Fig. S1. Spatial Pattern of Horizontal Land Motion (East-West) on Java Island. (A) Observed east-west velocities (2017 – 2023) across Java. The black rectangles in a show the extent of the zoomed in maps in b-d. Insets highlight areas of significant east-west motion in **(B)** Jakarta-Bekasi, **(C)** Bandung, and **(D)** Semarang-Demak. The underlying basemap in (A)–(D) , is provided by Esri, TomTom, Garmin, FAO, NOAA, USGS.

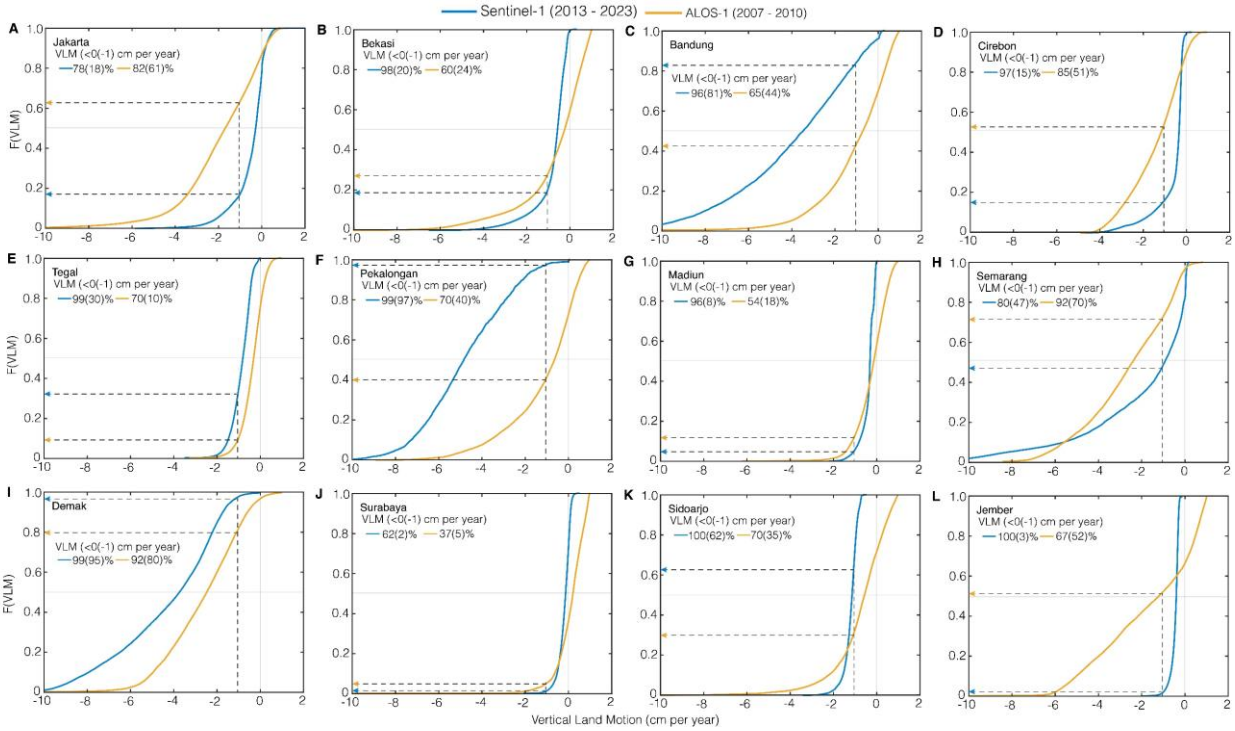

Fig. S2. Distribution of Vertical Land Motion (VLM) for major Cities on Java Island. Empirical cumulative distribution function of Sentinel-1 (blue lines) and ALOS-1 (yellow lines) for **(A)** Jakarta, **(B)** Bekasi, **(C)** Bandung, **(D)** Cirebon, **(E)** Tegal, **(F)** Pekalongan, **(G)** Madiun, **(H)** Semarang, **(I)** Demak, **(J)** Surabaya, **(K)** Sidoarjo, **(L)** Jember. The percentages in each city represent the percentage subsiding in each city.

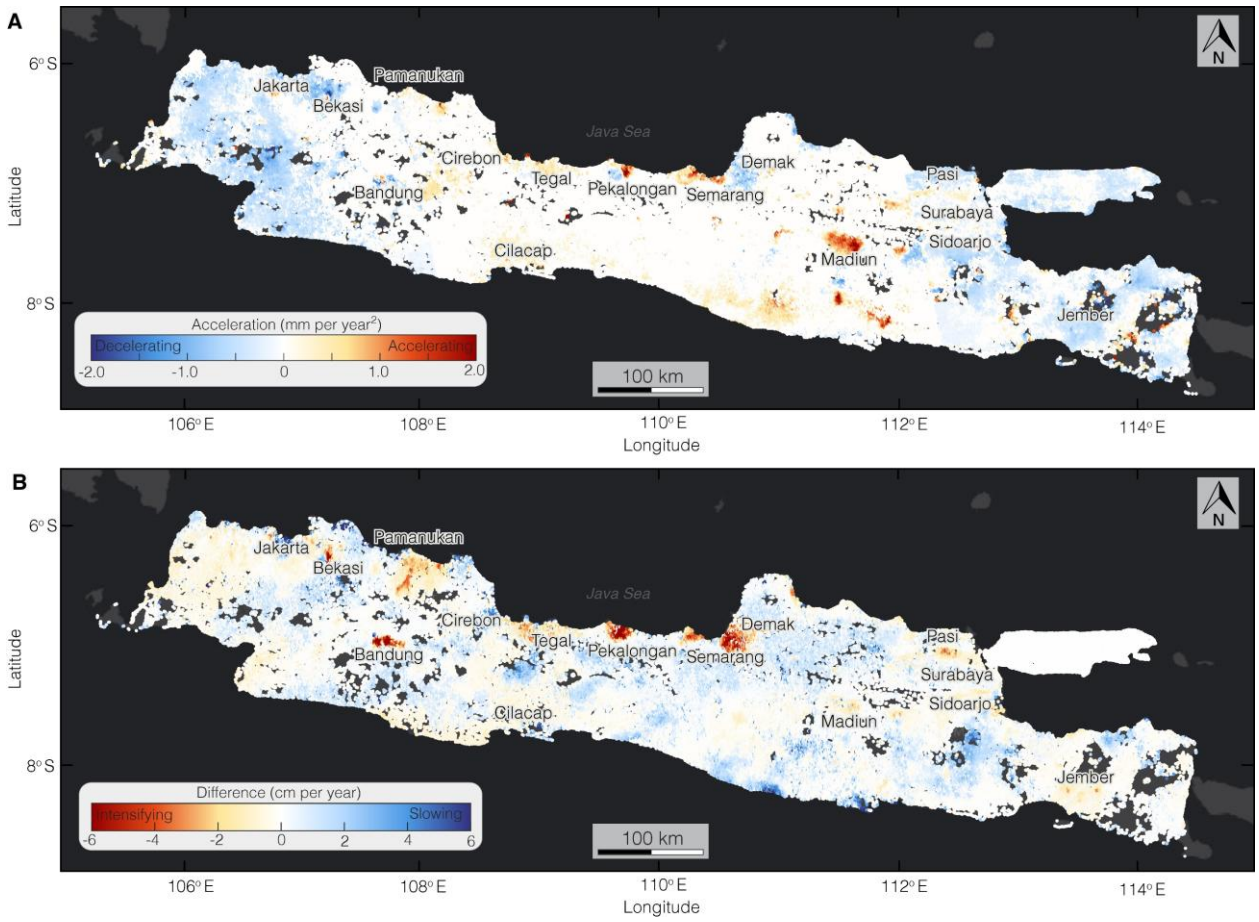

Fig. S3. Spatial Pattern of Vertical Land Motion (VLM) Trends on Java Island. (A) Short-term VLM trend analysis derived from Sentinel-1 (2017–2023) data using Equation 5. The positive values (red hues) indicate accelerating trends, the negative values (blue hues) indicate decelerating trends, while the white colors indicate linear trends. **(B)** Long-term VLM trend analysis derived from comparing Sentinel-1 and ALOS-1 using Equation 6. The positive values (blue hues) indicate slowing rates, the negative values (red hues) indicate intensifying rates, while the white colors indicate stable rates. The underlying basemap in (A) and (B), is provided by Esri, TomTom, Garmin, FAO, NOAA, USGS.

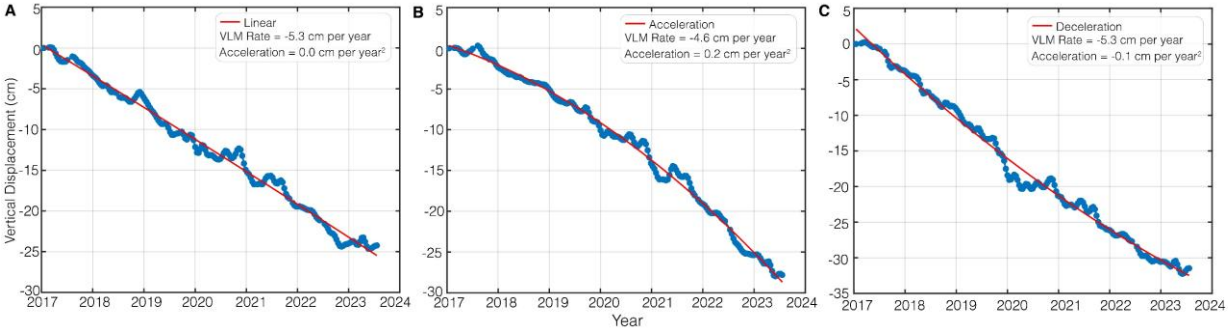

Fig. S4. Time Series of Short-term Vertical Land Motion (VLM) Trends. Representative time series of VLM showing **(A)** linear, **(B)** accelerating, and **(C)** decelerating trends. Blue circles represent observed vertical displacement; red lines show the fitted trend.

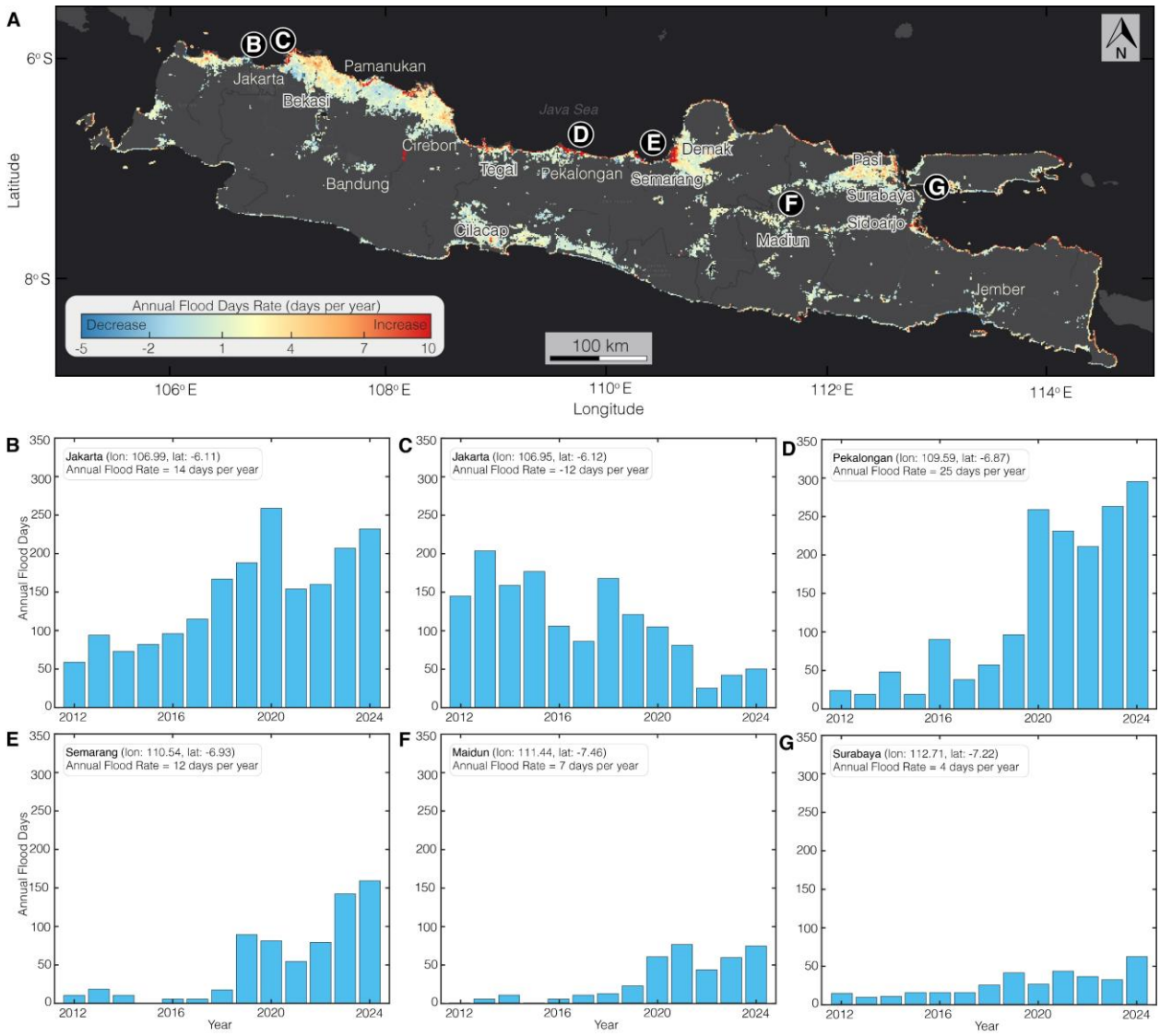

Fig. S5. Spatial and Temporal Patterns of Flood Exposure across Java Island.
(A) Spatial distribution of annual flood days rate between 2012–2024, showing regions of increase (red) and decrease (blue) in flood occurrence across Java. The flood data is derived from Visible Infrared Imaging Radiometer Suite (VIIRS) observations (*81*). Black circles (B–G) indicate selected urban hotspots. Time series of annual flood days from 2012–2024 at **(B, C)** Jakarta, **(D)** Pekalongan, **(E)** Semarang, **(F)** Madiun, and **(G)** Surabaya. The annual flood rates (gray boxes) are calculated as the average days per year over the study period. The underlying basemap in (A), is provided by Esri, TomTom, Garmin, FAO, NOAA, USGS.

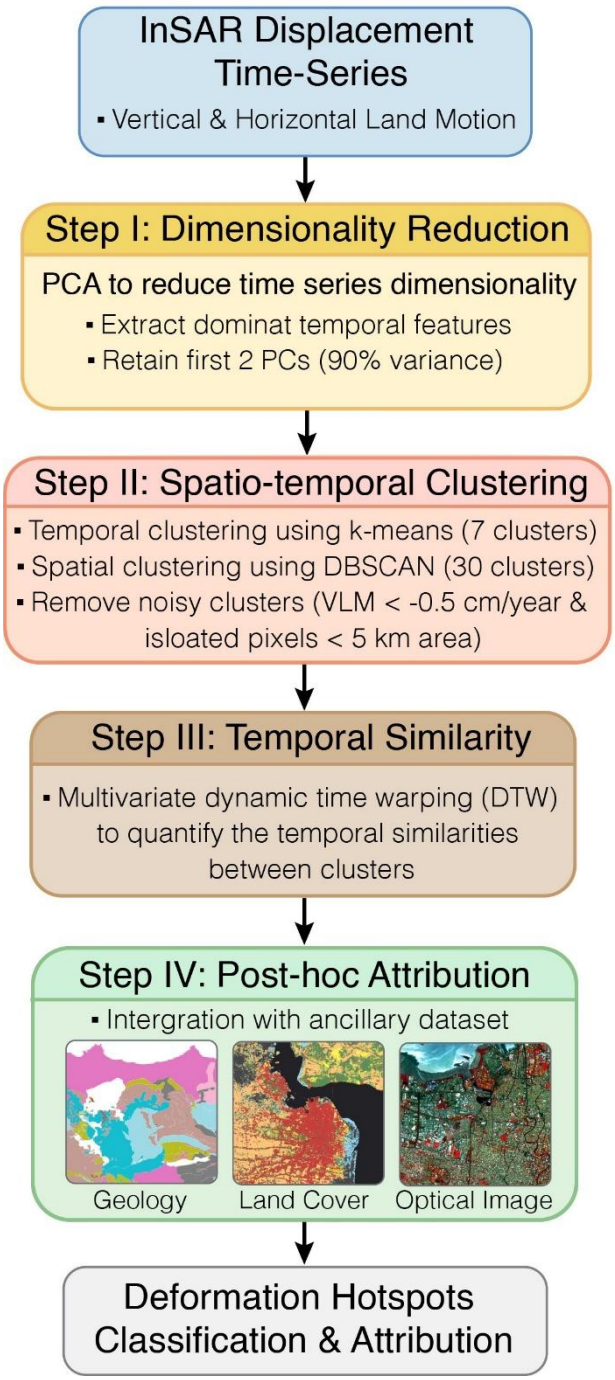

Fig. S6. Hybrid Unsupervised Machine Learning Method to Classify Deformation Hotspots. A four-step sequential approach starting with dimensionality reduction of the displacement time series, followed by temporal-spatial clustering and merging to derive cluster grouping that denote similar deformation trajectories, and finally *post-hoc* attribution to investigate drivers.

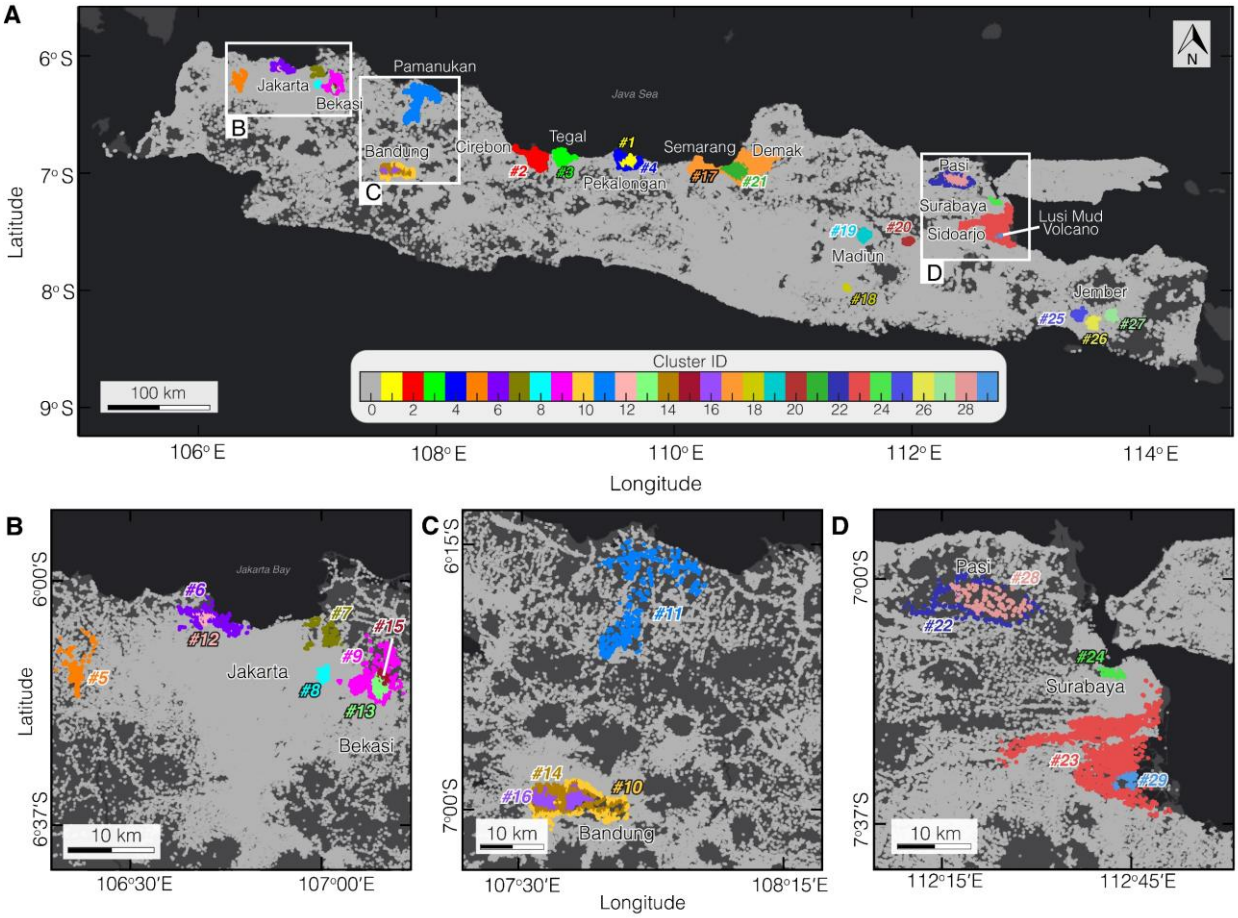

Fig. S7. Spatiotemporal Clustering of Land Deformation across Java Island. (A) Spatial distribution of subsidence hotspots derived using *k*-means clustering of InSAR-derived vertical land motion (VLM) time series and spatial coherence refinement using Density-Based Spatial Clustering of Applications with Noise (DBSCAN). There are 30 distinct clusters (color-coded) representing spatially coherent deformation patterns. This map extends from Fig. 3A. The black rectangles show the extent of the zoomed maps in B-D. Insets highlight multi-cluster regions in **(B)** Jakarta and Bekasi, **(C)** Bandung and Pamanukan, and **(D)** Surabaya and Sidoarjo. The underlying basemap in (A)–(D), is provided by Esri, TomTom, Garmin, FAO, NOAA, USGS.

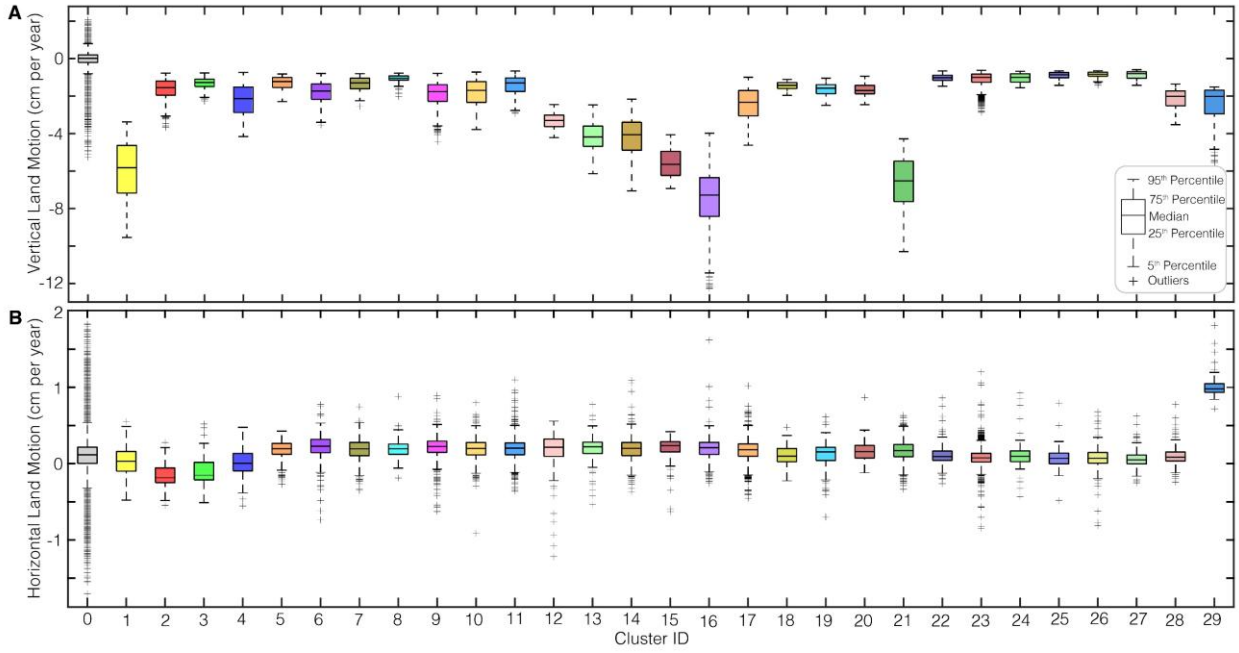

Fig. S8. Distribution of Spatiotemporal Clusters across Java Island. (A) Boxplots of vertical land motion (VLM) rates for the 30 clusters. **(B)** Boxplots of horizontal land motion (east-west) rates for the 30 clusters. The location and spatial extent of the clusters are shown in Supplementary Fig. 7A.

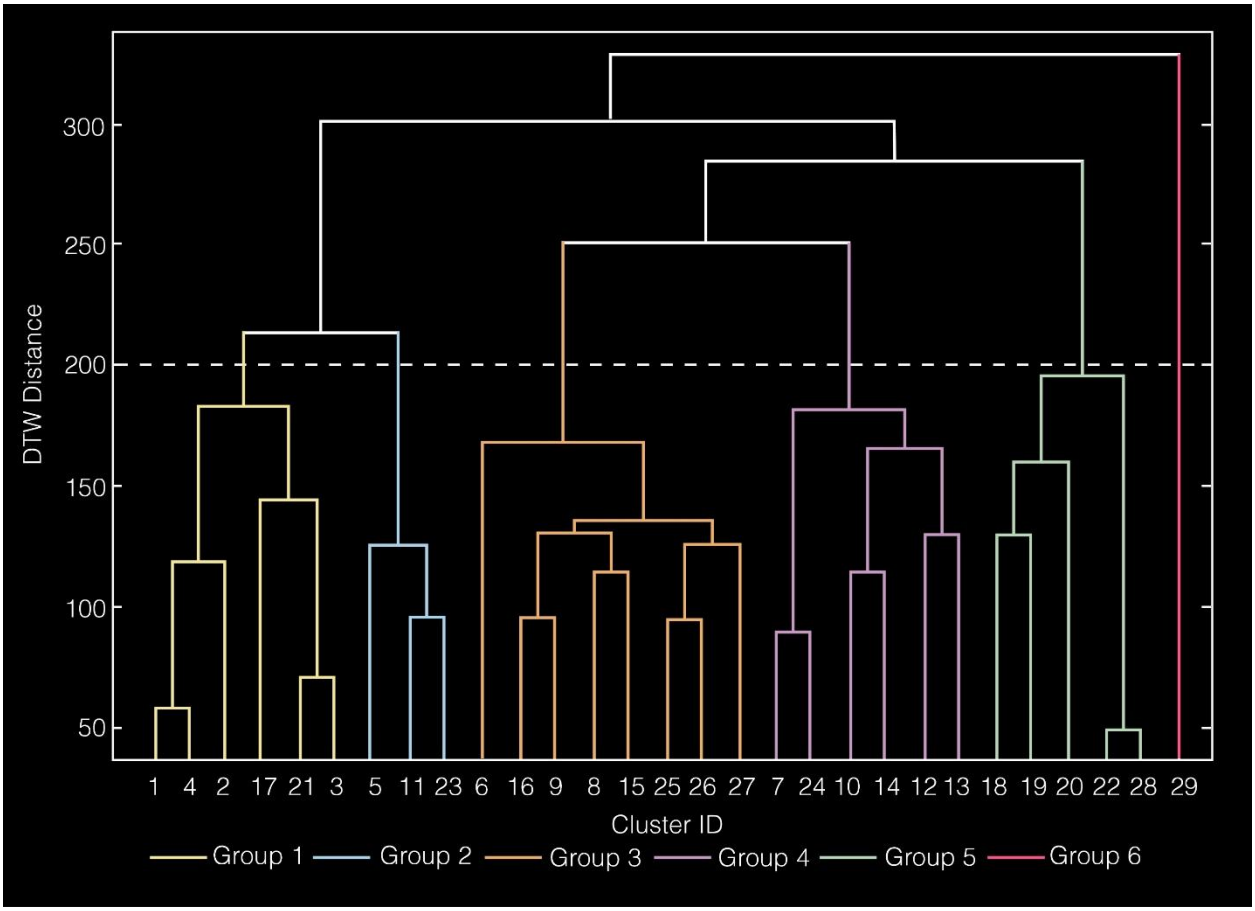

Fig. S9. Hierarchical Clustering of Clusters using Multivariate Dynamic Time Warping (DTW). Dendrogram illustrating the hierarchical clustering and temporal grouping of 29 clusters based on temporal similarity. The dendrogram highlights six major temporal groups (Groups 1–6) delineated at the selected DTW distance threshold (dashed white line), capturing distinct temporal deformation patterns across Java Island.

Fig. S10. Mean Temporal Trends of the Dynamic Time Warping (DTW) Groups across Java Island. (A) Mean vertical displacement time series for the six spatio-temporal groups identified through hierarchical clustering. **(B)** Corresponding mean horizontal displacement time series for the six spatio-temporal groups. The amplitude ratio legend indicates the relative vertical-to-horizontal displacement magnitude for each group. Amplitude ratios ≅ 1 indicate balanced deformation dynamics between vertical and horizontal displacements, amplitude ratios >1 indicate vertical deformation is the dominant deformation mode, while amplitude ratios <1 indicate horizontal deformation is the dominant deformation mode.

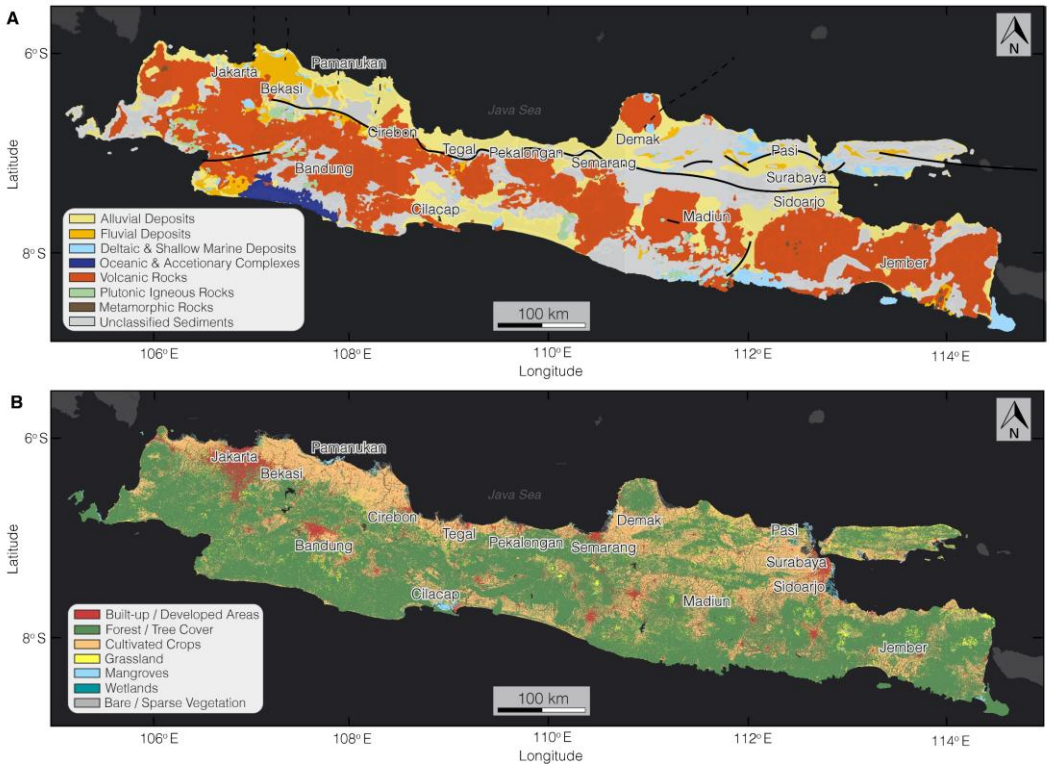

Fig. S11. Geological and land cover characteristics across Java Island. (A) Geological map of Java showing major surface lithologies. The thick solid black lines are active faults while the thin black dashed lines are Paleogene faults. The geology map was modified from the Indonesian Geospatial Agency dataset (*77*). The faults are modified after Aribowo et al. (*82*). **(B)** 2021 Land cover classification across Java showing diverse land-use types. The land use and land cover data were obtained from the European Space Agency (ESA) (*78*). The underlying basemap in (A) and (B), is provided by Esri, TomTom, Garmin, FAO, NOAA, USGS.

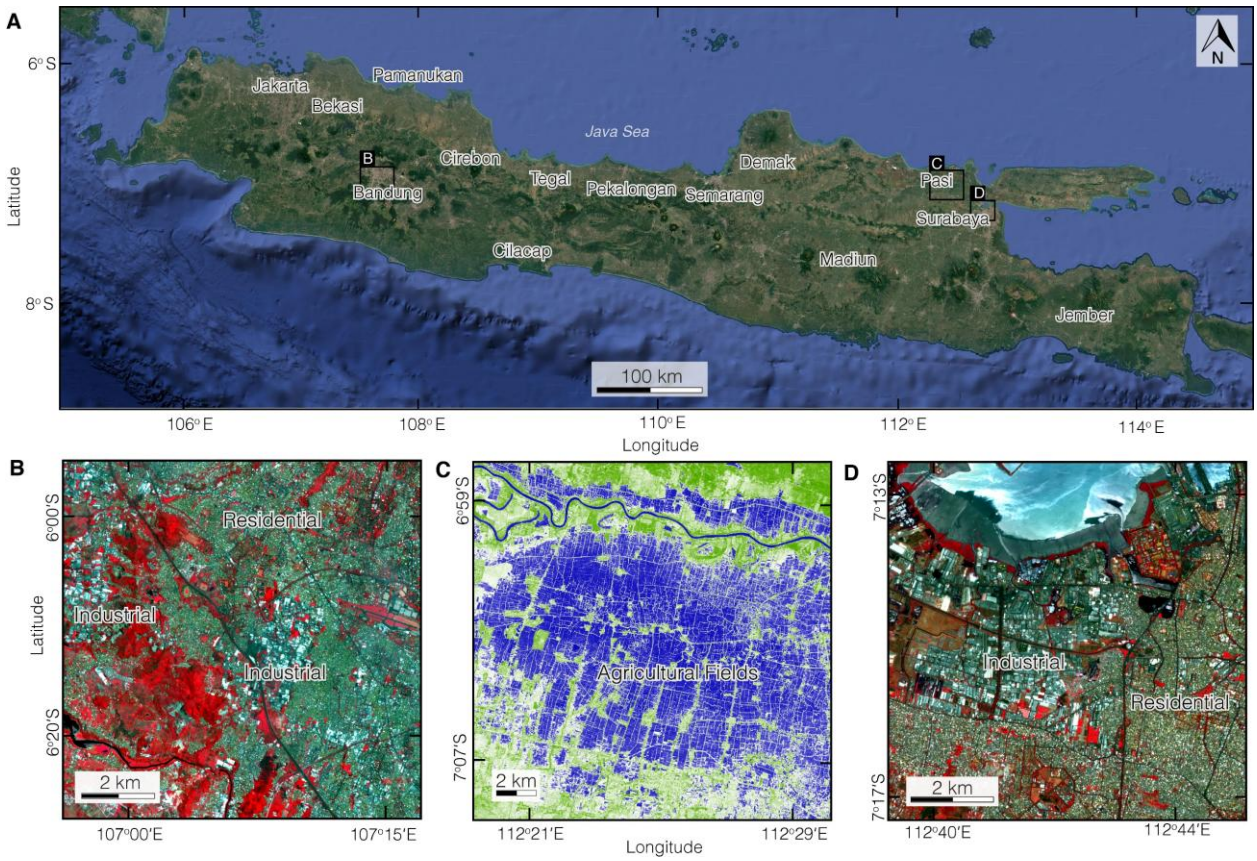

Fig. S12. Optical Satellite imagery across Java Island. (A) Google Earth satellite imagery of Java Island. Insets present representative examples from Sentinel-2 derived **(B)** false color composite (FCC) image over Bandung highlighting industrial areas (bright reflective roofs) and dense residential areas (heterogeneous, lower-reflectance surfaces), **(C)** normalized difference water index (NDWI) image over the agricultural fields and irrigation networks in Pasi (blue colors), and **(D)** FCC image over Surabaya showing extensive industrial zones and adjacent residential neighborhoods. The Sentinel-2 images are derived from Copernicus Data Space Ecosystem (https://browser.dataspace.copernicus.eu).

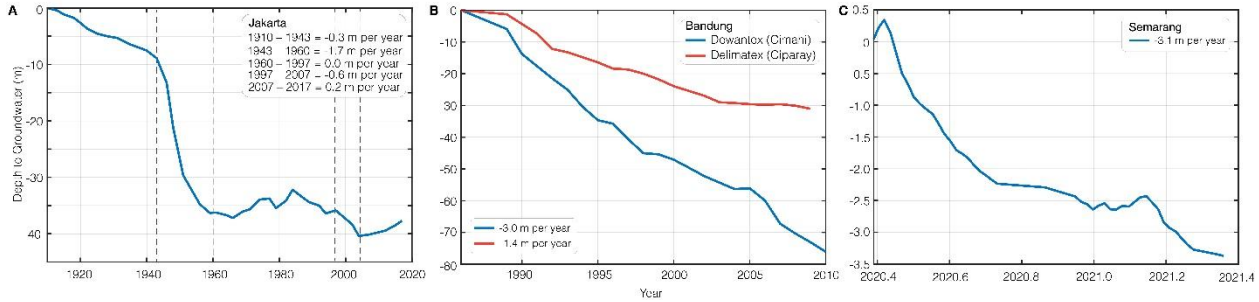

Fig. S13. Groundwater Level Trend in 3 Major Cities on Java Island. Groundwater level time series of **(A)** Jakarta (*83*), **(B)** Bandung (*29*), and **(C)** Semarang (*35*). Jakarta shows historical trends highlighting periods of accelerated decline, stability and upward trends, Bandung presents industrial well records at Dewanatex (Cimahi) and Delimatex (Ciparay), and Semarang shows recent rapid groundwater decline.

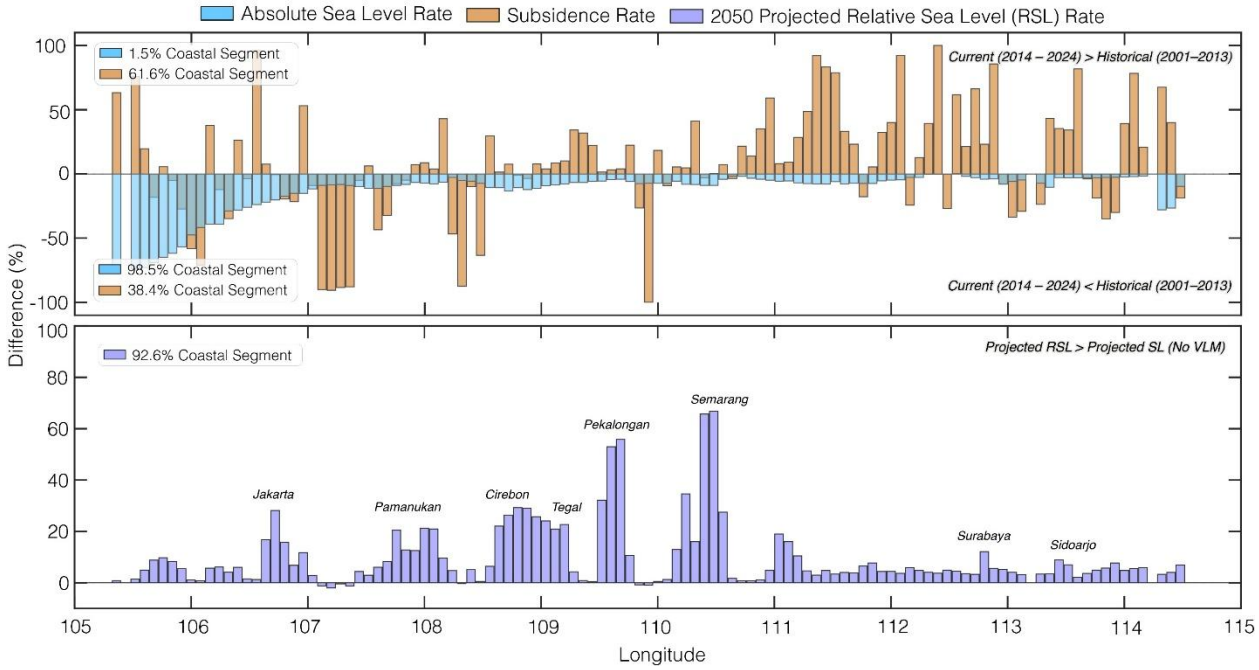

Fig. S14. Coastal Rate Differences in Sea Level and Vertical Land Motion (VLM) across Java Island. Differences in absolute sea level rates and VLM rates (top) between the historical period (2001–2013) and the current period (2014–2024), and projected 2050 relative sea level (RSL) rise rates compared to sea level rise rates without VLM (bottom) along the northern coastline. The projected rates are considered under shared socioeconomic pathways 2-4.5 (SSP2-4.5) scenario. The difference is expressed as a percentage, indicating the proportion of coastal segments with positive or negative changes (see panels) relative to the baseline: current period (top) and RSL (bottom).

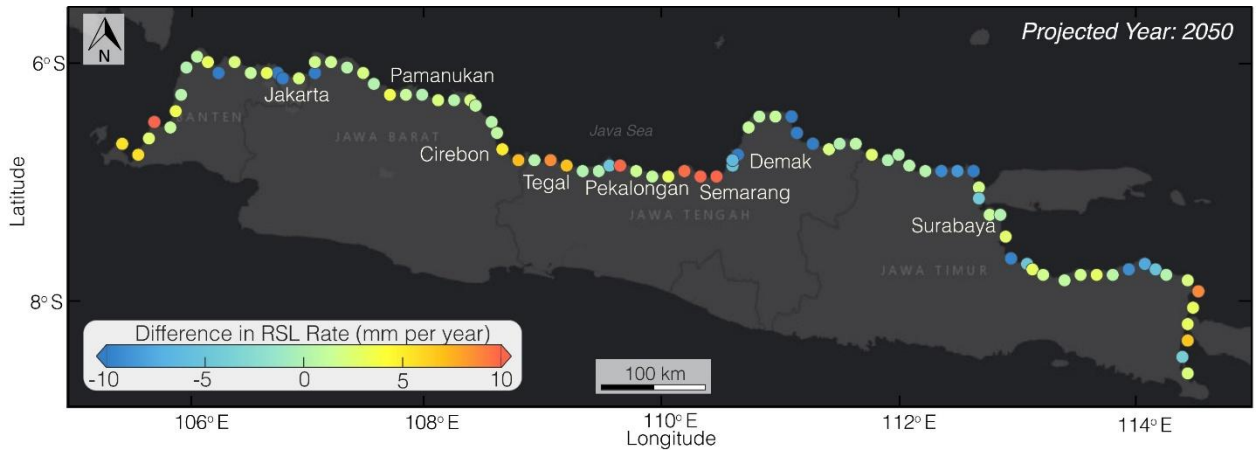

Fig. S15. Comparison of Projected Relative Sea-Level Rise (RSL) Rates along the Northern Coastline of Java Island. Differences in RSL rates considering linear versus non-linear (accelerations/decelerations) vertical land motion (VLM) rates for the year 2050. The projected rates are considered under shared socioeconomic pathways 2-4.5 (SSP2-4.5) scenario. Differences are expressed in mm per year along coastal segments, with color indicating the magnitude and direction of change. The underlying basemap is provided by Esri, TomTom, Garmin, FAO, NOAA, USGS.

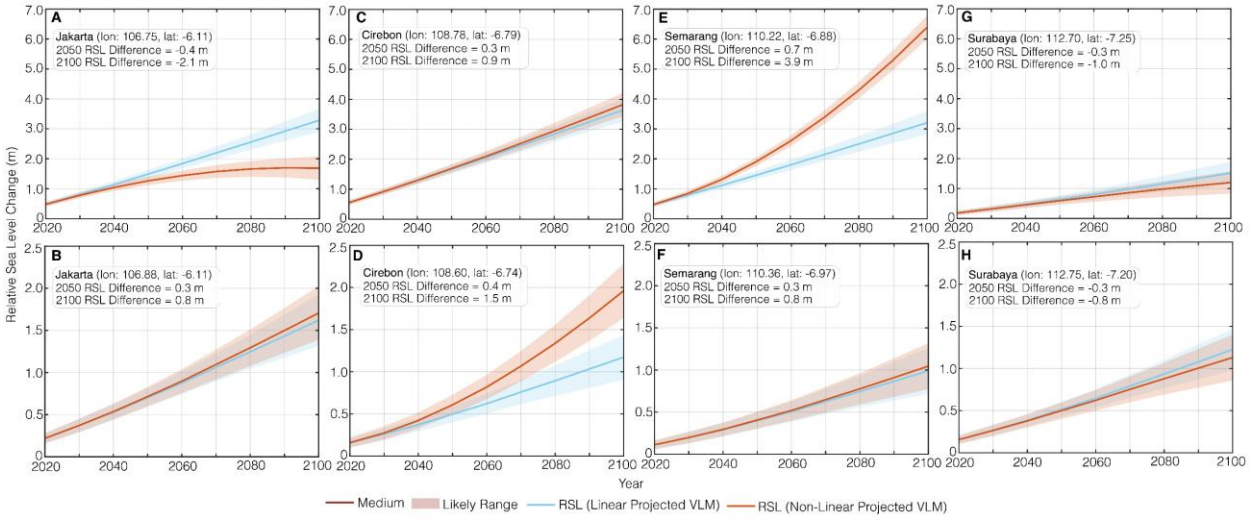

Fig. S16. Linear versus Non-Linear Projected Relative Sea-Level (RSL) Change for Selected Cities on Java Island. Comparison of projected RSL change considering linear (blue) versus non-linear (orange: accelerations/decelerations) vertical land motion (VLM) scenarios for **(A, B)** Jakarta, **(C, D)** Cirebon, **(E, F)** Semarang, and **(G, H)** Surabaya. The projections are evaluated under the shared socioeconomic pathways 2-4.5 (SSP2-4.5) scenario. Differences for the year 2050 are reported in each panel.

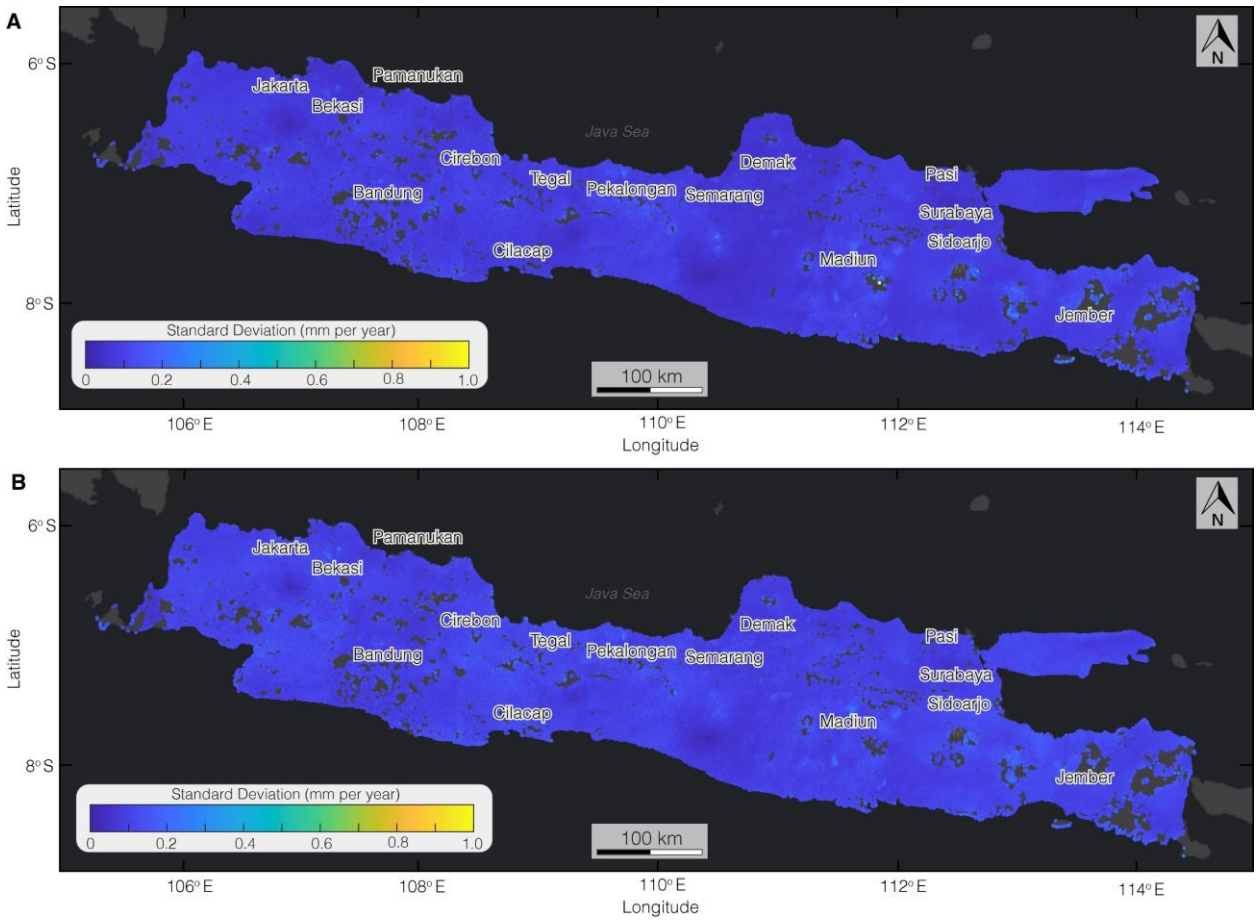

Fig. S17. Spatial Pattern of Standard Deviation on Java Island. Distribution of standard deviation for the **(A)** vertical land motion (VLM), and **(B)** east-west velocity. The underlying basemap in (A) and (B), is provided by Esri, TomTom, Garmin, FAO, NOAA, USGS.

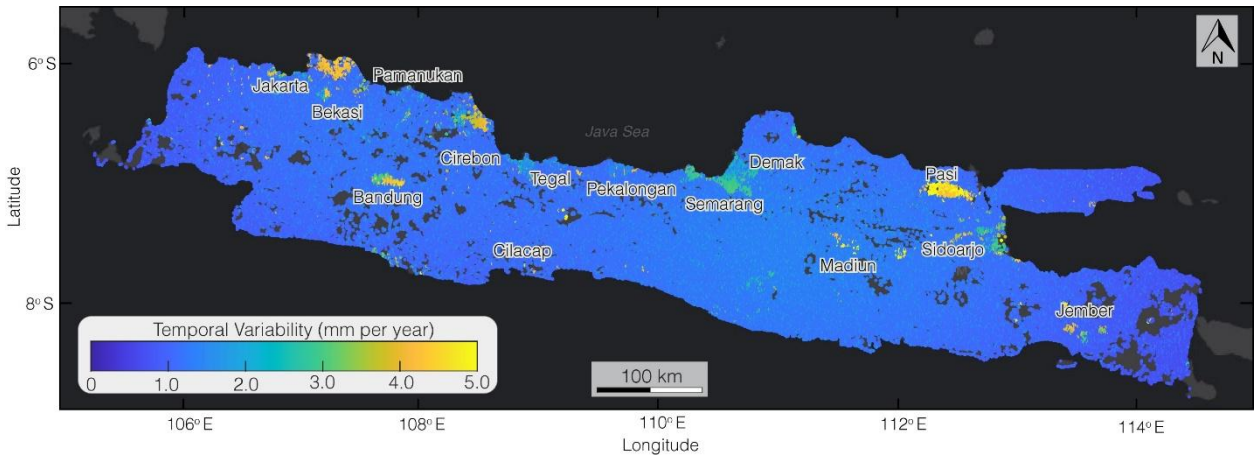

Fig. S18. Spatial Pattern of Temporal Variability on Java Island. Distribution of vertical land motion trend temporal variability. The underlying basemap is provided by Esri, TomTom, Garmin, FAO, NOAA, USGS.

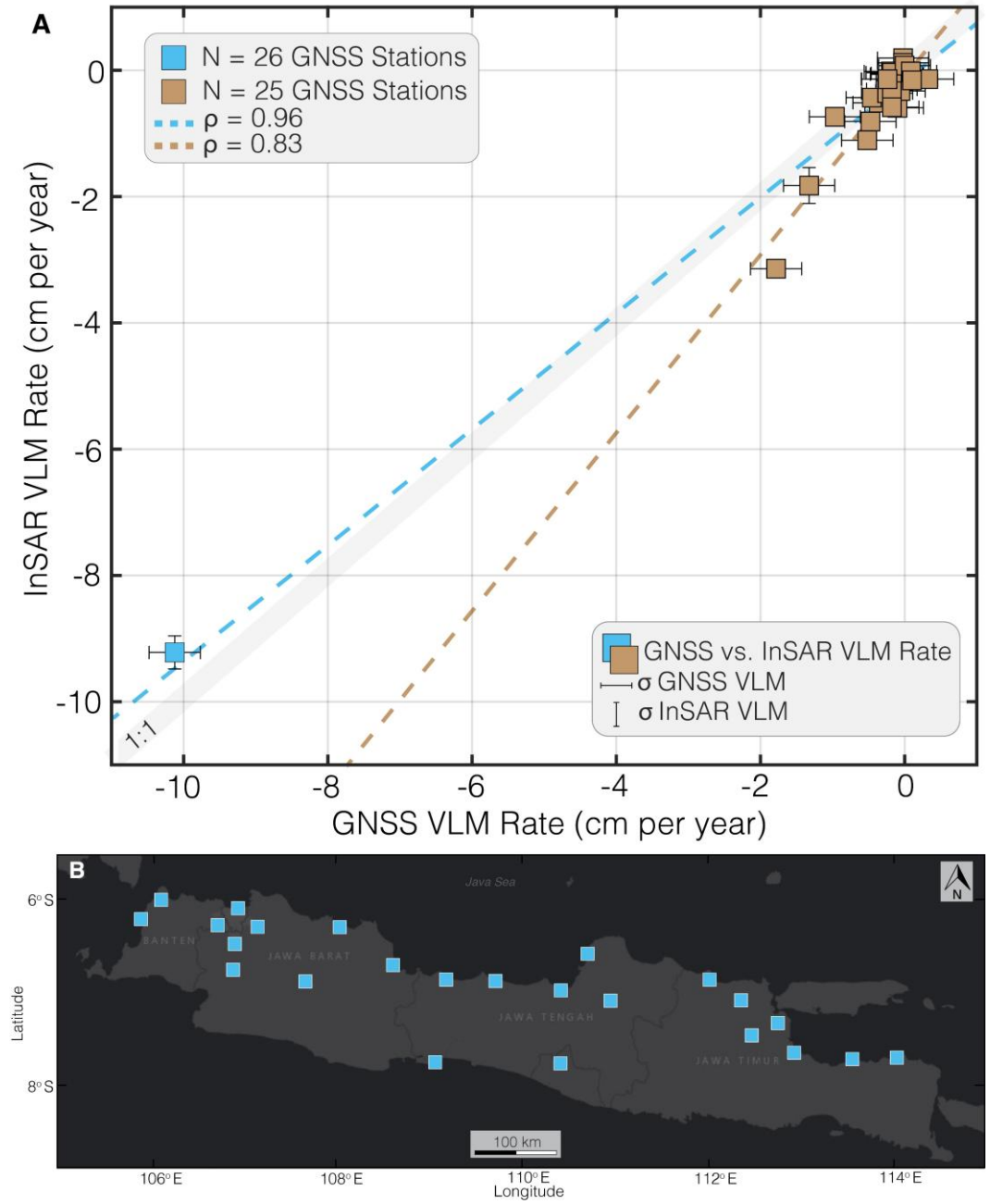

Fig. S19. Validation of Vertical Land Motion (VLM) on Java Island. (A) Bivariate plot comparing the global navigation satellite system (GNSS) vertical land motion (VLM) rates and interferometric synthetic aperture radar (InSAR) VLM rate. The blue dotted line represents the fit for the entire dataset, while the brown colors exclude the extreme point in blue. **(B)** GNSS stations used in the validation shown in **(A)**. The underlying basemap in (B), is provided by Esri, TomTom, Garmin, FAO, NOAA, USGS.

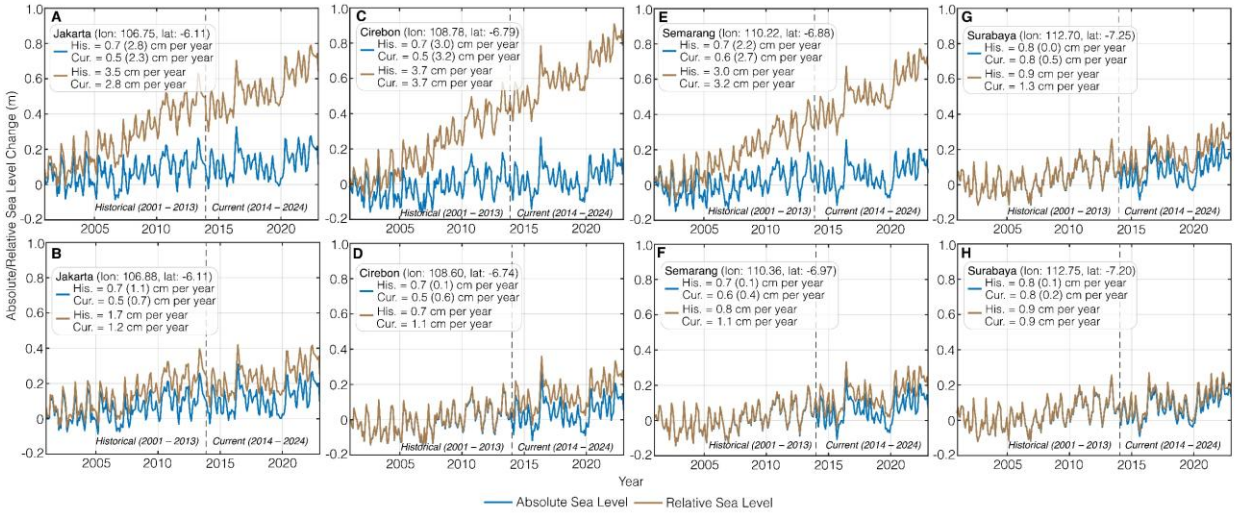

Fig. S20. Reconstructed Observed Monthly Sea-Level Trends for Selected Cities in Java Island. Reconstructed observed relative sea level (RSL) trends (brown lines) and observed absolute sea level (ASL) from satellite altimetry (blue lines) for **(A, B)** Jakarta, **(C, D)** Cirebon, **(E, F)** Semarang, and **(G, H)** Surabaya. The RSL trends were constructed using Equation 11. Panels show results of ASL, vertical land motion (VLM) in parentheses along with ASL, and RSL rates for historical (His. 2001–2013) and current (Cur. 2014 – 2024) periods. Note that RSL ≅ ASL + VLM for the different periods.

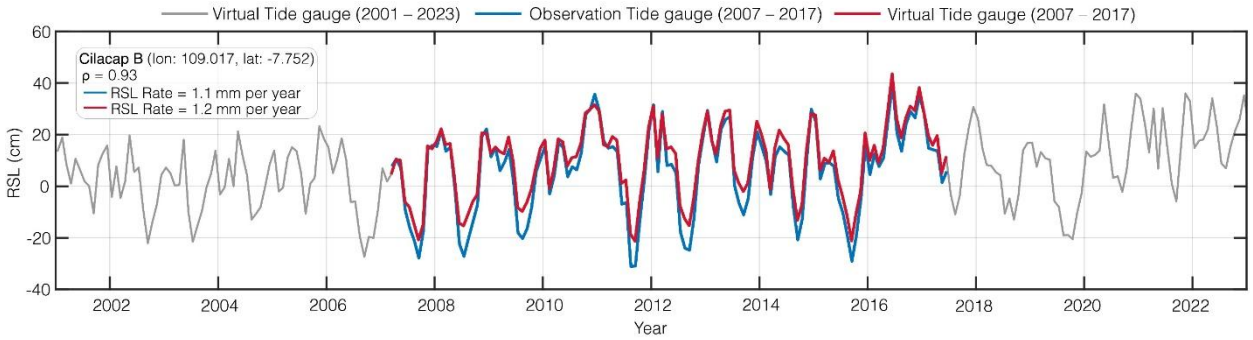

Fig. S21. Comparison of virtual and observed tide gauge records at Cilacap, Java Island. Time series of relative sea level (RSL) at Cilacap B showing virtual tide gauge data from 2001–2023 (gray), observed tide gauge measurements from 2007–2017 (blue), and virtual tide gauge data for the overlapping period 2007–2017 (red).

Table S1. Synthetic Aperture Radar (SAR) Datasets across Java Island. Summary of the ascending and descending orbits, paths, and 21 frames processed in this study.

<See attached Excel sheet>

Table S2. Summary of the Vertical Land Motion (VLM) rates for districts across Java Island. The population, average VLM, standard deviation for Sentinel-1 and ALOS-1 dataset for 122 districts on Java Island. The population data is based on the 2021 WorldPop Global High Resolution Population dataset (WPGP) available through https://www.worldpop.org/.

<See attached Excel sheet>

Table S3. Summary of spatiotemporal deformation groups across Java Island. Six deformation groups were identified using a hybrid unsupervised machine learning approach. This table summarizes the associated spatial clusters, deformation characteristics, surface geology, land use, and inferred subsidence drivers.

<See attached Excel sheet>

Data S1. Datasets for "Land Subsidence on Java Island and its Contributions to Relative Sea Level Change." (https://doi.org/10.5281/zenodo.15786356)